Aberrant neuronal connectivity in the cortex drives generation of seizures in rat Absence Epilepsy

Florian Studer, Guillaume Jarre, Benoit Pouyatos, Christian Nemoz, Elke Brauer-Krisch, Clémence Muzelle, Raphael Serduc, Christophe Heinrich, Antoine Depaulis

To cite this version:

Florian Studer, Guillaume Jarre, Benoit Pouyatos, Christian Nemoz, Elke Brauer-Krisch, et al.. Aberrant neuronal connectivity in the cortex drives generation of seizures in rat Absence Epilepsy. Brain - A Journal of Neurology , 2022, ⟨10.1093/brain/awab438⟩. ⟨hal-03437784⟩

HAL Id: hal-03437784
https://hal.science/hal-03437784v1

Submitted on 22 Nov 2021

Aberrant neuronal connectivity in the cortex drives generation of seizures in rat Absence Epilepsy

Journal:	*Brain*
Manuscript ID	BRAIN-2021-00897.R1
Manuscript Type:	Original Article
Date Submitted by the Author:	n/a
Complete List of Authors:	Studer, Florian; Univ.Grenoble Alpes, Grenoble Institut des Neurosciences, GIN; Inserm, U1216 Jarre, Guillaume; Univ.Grenoble Alpes, Grenoble Institut des Neurosciences, GIN; Inserm, U1216 Pouyatos, Benoit; Grenoble Institut des Neurosciences Nemoz, Christian; European Synchrotron Radiation Facility Bauer-Krisch, Elke; ESRF Muzelle, Clémence; ESRF Serduc, Raphael; Universite Grenoble Alpes, EA RSRM Heinrich, Christophe; Stem Cell and Brain Research Institute Depaulis, Antoine; INSERM, Grenoble Institut des Neurosciences
Methodology:	NEUROBIOLOGY OF DISEASE
Subject area:	EPILEPSY

Aberrant neuronal connectivity in the cortex drives generation of seizures in rat Absence Epilepsy

Florian Studer[1*], Guillaume Jarre[1], Benoit Pouyatos[1], Christian Nemoz[2], Elke Brauer-Krisch[2], Clémence Muzelle[3], Raphael Serduc[3], Christophe Heinrich[1,4,#] and Antoine Depaulis[1,5,#].

[#] These authors contributed equally to this work

Abstract:

Absence epilepsy belongs to genetic epilepsies and is characterized by recurrent generalized seizures that are concomitant with alterations of consciousness and associated with cognitive comorbidities. Little is known about the mechanisms leading to occurrence of epileptic seizures (i.e. epileptogenesis) and, in particular, it remains an open question whether neuronal hypersynchronization, a key feature in seizure initiation, could result from aberrant structural connectivity within neuronal networks endowing them with epileptic properties. In the present study, we addressed this question using a genetic model of absence epilepsy in the rat where seizures initiate in the whisker primary somatosensory cortex. We hypothesized that alterations in structural connectivity of neuronal networks within wS1 contribute to pathological neuronal synchronization responsible for seizures. First, we used rabies virus-mediated retrograde synaptic tracing and evidenced that cortical neurons located in both upper- and deep-layers of whisker primary somatosensory cortex displayed aberrant and significantly increased connectivity the genetic model of absence epilepsy, as highlighted by a higher number of presynaptic partners. Next, we showed at the functional level that disrupting these aberrant whisker primary somatosensory cortex neuronal networks with synchrotron X-ray-mediated cortical microtransections drastically decreased both whisker primary somatosensory cortex neuron synchronization and seizure power, as revealed by *in vivo* local field potential recordings with multichannel probes. Taken together, our data provide for the first time strong evidence that increased structural connectivity patterns of cortical neurons represent critical pathological substrates for increased neuronal synchronization and generation of absence seizures.

Author affiliations:

[1] Univ. Grenoble Alpes, Inserm, U1216, Grenoble Institut Neurosciences, 38000 Grenoble, France

[2] Biomedical Beamline, European Synchrotron Radiation Facility, ESRF, 38000 Grenoble, France

[3] Univ. Grenoble Alpes, Inserm UA7, STROBE, 38000 Grenoble, France

[4] Univ Lyon, Université Claude Bernard Lyon 1, Inserm, Stem Cell and Brain Research Institute U1208, 69500 Bron, France

[5] Centre Hospitalier Universitaire Grenoble Alpes, 38000 Grenoble, France

[*] Present address: Department of Biomedicine, University of Basel, Basel, Switzerland

Correspondence to: Dr. Antoine Depaulis

Grenoble Institute of Neuroscience

Chemin Fortuné Ferrini

38700 La Tronche, France

E-mail : antoine.depaulis@univ-grenoble-alpes.fr

Correspondence can also be addressed to: Dr. Christophe Heinrich

Stem Cell and Brain Research Institute

18 avenue Doyen Lépine

69500 Bron, France

E-mail: Christophe.heinrich@inserm.fr

Running title : Cortical connectivity in absence seizure

Key words: somatosensory cortex; absence epilepsy; neuronal synchronization; synchrotron microtransections; rabies virus synaptic tracing

Abbreviations: Al: aluminum; AP: antero-posterior; Be: beryllium; BSA: bovine serum albumin; C: carbon; CSD: current-source density; Cu: cuivre; DV: dorso-ventral; ECoG: electrocorticogram; EnvA: avian sarcoma leucosis virus envelop A; FFT: fast Fourier transform; G: rabies glycoprotein; GAERS: Genetic Absence Epilepsy Rats from Strasbourg ; GAERS-SI: synchrotron-irradiated Genetic Absence Epilepsy Rats from Strasbourg; GFAP: glial fibrillary acidic protein; GFP: green fluorescent protein; Gy: gray; Iba1: ionized calcium binding adaptor molecule 1; L: cortical layer; LFP: local field potential; LV: lentivirus; ML: medio-lateral; MUA: multi-unit activity; NeuN: neuronal nuclei; PFA: paraformaldehyde; RABV: rabies virus; RECA: anti-endothelial cell antibody; RT: room temperature; SEM: standard error of the mean; SEP: sensory-evoked potentials; SWD: spike-and-wave discharge; TVA: avian tumor virus receptor A; VSV-G: vesicular stomatitis virus-glycoprotein; wS1: whisker primary somatosensory cortex.

Introduction

Neocortical connectivity and network activity have been extensively studied both structurally [1,2] and functionally [3–5] in order to understand the coding of physiological functions. In particular, sensory cortices display a stereotyped structural and functional connectivity that allows for proper perceptual sensory coding [6]. The whisker primary somatosensory cortex (wS1) has been a heuristic model because of its stereotyped organization and its key role in the integration of sensory information in rodents. Each cortical column in wS1 processes information from one whisker through a canonical neuronal circuit [7,8] whose activity is modulated by local microcircuits [9]. Yet, whether altered neuronal connectivity within this network can lead to impaired functioning, as observed in some brain pathologies such as epilepsy [10–12], is a critical issue. In particular, it remains an open question whether neuronal hypersynchronization, which is a key feature in the initiation of epileptic seizures [13], could result from aberrant anatomical connectivity within cortical networks.

In the present study, we addressed this question in the context of absence epilepsy [14], a prototypical form of generalized epilepsy, which is characterized by recurrent seizures consisting of spike-and-wave discharges (SWDs) that are initiated in the cortex in human patients and animal models [15–19]. The Genetic Absence Epilepsy Rats from Strasbourg (GAERS) is a well-established absence epilepsy model [20], based on the selection of rat showing spontaneous SWDs that recapitulates most electrophysiological, behavioral and pharmacological features of human Absence Epilepsy [21,22]. In addition, a gain of function mutation on the CACNA1H gene was found in GAERS [23] which is similar with mutations found in human patients [24–26]. Using this model, we previously showed that spontaneous SWDs are initiated in wS1 [27], and that deep layer pyramidal neurons of this cortical region exhibit fast activation, hyperexcitability and hypersynchronizing properties, hence suggesting that they could play a critical role as ictogenic neurons in absence seizures [17,28].

Here, we hypothesized that alterations in structural connectivity of cortical neuronal networks within wS1 (i.e. seizure initiation area) could contribute to the pathological neuronal hypersynchronization responsible for SWDs. First, to unravel neuronal epileptic networks in GAERS, we used rabies virus (RABV)-mediated retrograde synaptic tracing [29–31], and evidenced that cortical neurons located in both upper- and deep-layers of wS1 displayed aberrant and significantly increased connectivity in GAERS, including enhanced innervation by GABAergic interneurons. Next, we showed at the functional level that disrupting these neuronal networks with synchrotron X-ray-mediated cortical microtransections [32,33] drastically reduced both neuronal synchronization and seizure power, as revealed by *in vivo* multielectrode electrophysiological recordings. Taken together, our data provide strong evidence that structural alterations in connectivity patterns of cortical neurons within wS1 represent critical pathological substrates for increased neuronal synchronization and generation of absence seizures in GAERS rats.

Materials and Methods

Experimental subjects

All protocols were approved by local Ethical Committees (Ethax and Grenoble Institute of Neuroscience) and the French Ministry of Research, and experiments were carried out in accordance with European Union guidelines (directive 2010/63/EU). Adult GAERS male rats (2-3 months old at the time of surgery or synchrotron-generated cortical microtransections) of the Grenoble colony and age-matched control non-epileptic Wistar rats (Charles River, L'Arbresle, France) were used to perform these experiments. 9 GAERS, 7 synchrotron-irradiated (SI) GAERS (referred to as GAERS-SI) and 9 Wistar rats were used for RABV experiments. 5 GAERS and 6 GAERS-SI were used for freely-moving LFP recordings. 5 GAERS and 6 GAERS-SI were used for silicon-probes recordings. 8 GAERS and 10 GAERS-SI were used for behavioral tests among which 3 of each group were used for histological characterization of synchrotron cortical microtransections. They were maintained with food and water *ad libitum* in a 12:12h light dark cycle with light on at 7:00 am, at a temperature of 24 ± 2°C. Rats implanted for freely-moving LFP recordings were housed individually to avoid the deterioration of the connector. For other experiments, rats were housed in groups of 2 to 4.

Rabies virus neuronal connectivity tracing

The rabies virus was pseudo-typed with the EnvA avian protein, that is specific to the TVA receptor, and G-protein deleted. The RABV tracing method is based on the EnvA/TVA pseudo-typing and the G trans-complementation [34] which restrict the subsequent retrograde tracing. EnvA expression constrains RABV infection in TVA expressing neurons only and G allows the spread of RABV to the first-order pre-synaptic partner.

Rats were anesthetized as previously described with mixed ketamine and xylazine and were stereotaxically injected in the wS1 (AP: -2; ML: 5.5 mm from bregma; DV: -0.25 mm from brain surface for L2/3 neurons targeting; DV: -1.8 mm from brain surface for L5/6 targeting) with a lentivirus encoding TVA, G and histone-GFP driven by a human synapsin neuronal promoter (pBOB-synP-HTB, Addgene plasmid # 30195) with a glass micropipette controlled by a nanoinjecter (120nL, 30nL/min) (NanoLiter 2010, WPI, Sarasota, FL, USA) (Fig. 1A). After injection, the micropipette was left in place for 5 min. This first injection permitted the restriction of subsequent retrograde tracing arising from the wS1. Fourteen days later, the same animals were anesthetized with the same protocol and stereotactically injected, as for LV, with a modified rabies virus (EnvA-G-deleted-RabiesmCherry, Salk Institute, titer: 1.3×10^9/ml, 120nL, 30nL/min), pseudo-typed with the EnvA, deleted for the glycoprotein G and encoding mCherry (Fig. 1A). Seven days later, animals were euthanized and their brain collected for analysis.

Only animals with a majority of starter cells (i.e. co-infected cells: expressing both GFP and mCherry) located in the targeted cortical cell layer, i.e. L2/3 (>80%, Supplementary Fig. 1B) or L5/6 (>95%, Supplementary Fig. 1C), were kept for analysis. The location of presynaptic partners was listed every 2 brain sections. The connectivity quantification is expressed as the ratio of the number of presynaptic neurons (mCherry+), in a cell layer of wS1 or more distant brain areas, over the total amount of starter cells (GFP+/mCherry+).

Lentivirus production

We used lentiviral vectors pseudotyped with VSV-G (Vesicular Stomatitis Virus-Glycoprotein). VSV-G pseudotyped lentiviral vectors were produced using standard triple-transfection using 293T cells as packaging cell line. Lentiviral particles were concentrated from supernatants of transfected packaging cells by ultracentrifugation following standard protocols, and resuspended in a buffer containing 50 mM Tris-HCl pH 7.8, 130 mM NaCl, 10 mM KCl, and 5 mM MgCl2. Viral particles were frozen and stored at -80°C until use.

Synchrotron X-ray cortical microtransections

Cortical microtransections were performed at ID17, the biomedical beamline of the European Synchrotron Radiation Facility (ESRF, Grenoble, France). X-rays were produced from a 1.6T wiggler located at 43 m from the sample. The white beam was filtered with Be (0.5 mm), C (1.5 mm), Al (1.5 mm) and Cu (1.0 mm) resulting in a pink spectrum extending from 50 to 350 keV (median energy: 107 keV). The dose rate in air at the animal surface was approximately 16,000 Gy.s^{-1}. We performed synchrotron irradiation as previously described [35,33]. GAERS were anesthetized as for surgery (see above) and positioned on a rotation stage placed above a goniometer and low dose X-ray projections images [36] of the rat head were first acquired to delineate the irradiation fields defined from the bregma, as previously described [32] (+45° from horizontal, antero-post: 0 to -4 mm, medio-lateral: + 5.5 mm centered, dorso-ventral: 2.5 mm centered on -2mm). Each transection was then performed by one single 50 µm-thick microbeam entering the brain through 1 irradiation ports with an angle of 45° from the surface of the skull to specifically irradiate unilaterally the targeted brain area. Eleven, 400-µm spaced apart, transections were performed between 0 mm and − 4 mm from the bregma to cover the wS1. The microbeam entrance dose computed using PENELOPE-2006 Monte Carlo code was 540 Gy, defined as the optimal range for axonal lesions [37].

Immunohistochemistry and image analysis

Animals were euthanized with an overdose of pentobarbital (200 mg/kg, i.p.) and transcardially perfused with PBS followed by 4% PFA. The brains were then removed from the skull, postfixed (4% PFA, 4°C, overnight), cryoprotected (30% sucrose, 4°C, 2 days), frozen in isopentane (-40°C, 1 min) and finally cut in coronal or horizontal sections (40-µm thickness). Free-floating sections were first washed in PBS (3x15 min) and then saturated and permeabilized in 0.25% triton X-100, 2% BSA in PBS (1h, room temperature). Primary antibodies (Supplementary Table 1) were then incubated in 0.1% triton X-100, 2% BSA in PBS (4°C, overnight). ~~The following primary antibodies were used: anti-Neuronal Nuclei (NeuN, mouse, 1:500, Merck Millipore), anti-CDP (Cux1, rabbit, 1:250, Santa Cruz), anti-CTip2 (rabbit, 1:250, Abcam), anti-RFP (mouse, 1:500, Abcam), anti-GFP (chicken, 1:250, Abcam), anti-γ-amino-butyric acid (GABA, rabbit, 1/250, Sigma-Aldricht), anti-CD68 (mouse, 1/500, Antibodies online), anti-GFAP (rabbit, 1/500, Agilent Technologies), anti-RECA (mouse, 1/500, Bio Rad), anti-NEFH (neurofilament, mouse, 1/1000, ThermoFischer Scientific), anti-Olig2 (mouse, 1/500, Abcam).~~ After extensive washing in PBS (3x15 min), sections were incubated with appropriate species or subclass-specific secondary anti-bodies (Supplementary Table 1) ~~conjugated to FITC (Fluorescein, 1:500, Jackson ImmunoResearch Laboratories), Alexa Fluor 488, 555, 647 (1:500, Life Technologies)~~ in the dark (2h, RT) followed by Hoechst staining (1:2000, 5 min, RT, Invitrogen). Finally, brain sections were extensively washed (3x15 min) and mounted onto glass slides, air-dried and coverslipped with anti-fading mounding medium (Aqua Moly/Mount; Polysciences, Warrington, PA, USA).

Confocal images were acquired using an inverted confocal microscope (LSM 710, Zeiss) and analyzed using ImageJ (NIH, USA). Cortical layer boundaries were based on Cux1 and CTip2 immunolabelling and Hoechst staining (Supplementary Fig. 1A). Cellular densities and fluorescence intensity were estimated for the wS1 cortex [38] based on the expression of specific markers (NeuN, RECA, Hoechst, GFAP, Iba1) on horizontal brain sections using MoreHisto, an ~~in-house~~ automated histological quantification program (MoreHisto, Meylan, France). For each animal (n=3 / group), we estimated the cell density/fluorescence intensity in three different slices and the average of the three values was used for statistical comparison between groups.

LFP recordings in freely-moving rats

Surgery.

For chronic Local Field Potential (LFP) recordings, GAERS rats were stereotaxically implanted in the wS1 with bipolar electrodes (Enamelled copper wire, Ø 220 µm, Block, Verden, Germany) while anesthetized with a mixture of xylazine (5-10 mg/kg i.p.; Rompun®, Centravet, Dinan, France) and ketamine (40-100 mg/kg i.p.; Clorketam1000®, Vetoquinol, Centravet, Dinan, France). Incisions and compression points were infiltrated with lidocaine

(2%; Centravet, Dinan, France). Stereotaxic coordinates were antero-posterior from bregma (AP): -2.5 mm; medio-lateral (ML): -5.5 mm; dorso-ventral (DV): -2.5 mm [38]. A stainless-steel screw (Ø 1mm) inserted over the cerebellum served as a reference electrode. All electrodes were soldered to a female microconnector (BLR150Z; Fischer Elektronik, Lüdenscheid, Germany) and secured on the animals' head with dental cement.

Video-LFP recordings.

After a post-surgery recovery period of one week, LFP were acquired from freely-moving rats with a digital acquisition system (Coherence 3NT, Deltamed, Paris, France) at a sampling rate of 1,024 Hz and an analog bandpass filtering between 1 and 256 Hz, synchronized with video. Rats were recorded for at least 60 min every other week from 2 weeks after synchrotron irradiation and up to 2 months. The occurrence of cortical discharges on LFP recordings was always confirmed with the video to distinguish epileptiform events from physiological activity patterns associated with sleep, exploratory behaviour or grooming. At the end of experiments, animals were killed with an overdose of pentobarbital (200 mg/kg i.p.) and brains were removed, frozen at -40°C in isopentane and cut in coronal sections for histological processing to verify electrodes' location.

LFP recordings analysis.

Time-frequency and spectral analysis of cortical discharges were performed using ImaGIN, an open source SPM toolbox for intracranial EEG (https://f-tract.eu/software/imagin/) written in Matlab (The MathWorks, MA, USA) for Fast Fourier Transforms (FFT) and Morlet wavelet transforms of intracortical LFPs as previously described [33]. Briefly, for each SWD, time-frequency analysis of SWD power were computed between 4 and 20Hz with a 0.1 Hz step. The mean baseline power was used to normalize individual SWD in amplitude. The time axis of the time-frequency chart was linearly rescaled to realign the start and end of SWD with a time resolution of 0.1s to allow statistical analyses of signal in the time-frequency plane over all SWD duration [33]. Fast-Fourier Transforms (FFT) of interictal signal were computed and the FFT amplitude was averaged in each frequency band.

Silicon probes recordings

Surgery.

GAERS rats were initially anesthetized for surgery with ketamine and xylazine, as mentioned above, and then immobilized with D-tubocurarine hydrochloride pentahydrate (0.4mg/kg, i.p.; Sigma-Aldrich, Saint-Quentin Fallavier, France) and artificially ventilated. They were maintained in a sedated state by repeated injections of fentanyl (1µg/kg, i.p.; Janssen-Cilag, Issy les Moulineaux, France). This preparation allows the recording of immobilized GAERS in a quiet-wakefulness state prone to SWD occurrence and similar to what is observed when they are freely moving [21]. A craniotomy was done over the wS1 cortex to allow the insertion of a linear silicon probe (16 channels, 15 µm site Ø, 150 µm inter-site distance; Neuronexus technologies, Ann Arbor, MI, USA) (n=10). The insertion depth of the silicon probes was controlled through a micromanipulator. Post-hoc detection of polarity reversion in infragranular layers [39] associated with DiI application on the back of the probes (Supplementary Fig. 3A) was used to assess the location of each recording sites in the different cortical layers. A tin electrode was also positioned on the dura within the boundaries of the craniotomy, near the silicon probe, to record wS1 ECoG activity.

Recordings.

Signal was amplified through two miniature preamplifiers (MPA8i, Multichannel System, Reutlingen, Germany) connected to a 32-channel programmable gain amplifier (PGA-32, voltage gain, x200 Multi Channel Systems, Reutlingen, Germany) and sampled at 20 kHz (16 bit ADC). Recordings were collected on a personal computer *via* a CED interface (Cambridge Electronic Design, Cambridge, UK) using the Spike 2 software.

Sensory evoked potentials (SEP).

Sensory responses were evoked by air-puffs (50 ms) timed by a pressure device (PMI-200, Dagan, Minneapolis, MN, USA) and delivered to the contralateral whiskers, as previously described [27]. Air-puffs, which deflected four to eight whiskers by ∼10 degrees [40,41], were applied 60–100 times every 0.24 Hz. At the beginning of each experiment, the orientation and pressure (10-20 psi) of the air puff was adjusted for each experiment to generate a SEP of maximal amplitude.

Silicon probes recordings analysis.

Raw signal was bandpass filtered (0.1-100Hz) for current source density (CSD) analysis. CSD analysis was performed to detect extracellular sources and sinks in wS1 layers as previously described [27]. CSD was computed on each recording site as the second spatial derivative [42]. Multi-unit activity (MUA) was detected as negative event ≥ 2 SD of the baseline on the bandpass filtered trace (0.6-6kHz). LFP and MUA analysis were done using custom-written Matlab scripts and the Spike2 software (CED, Cambridge Electronic Design, Cambridge, UK).

Behavioral tests

Openfield and Rotarod tests were used to detect sensorimotor side-effects of synchrotron irradiation [32]. We used an accelerating paradigm (4–40 rpm, 5 min) on the Rotarod (Panlab/Harvard Apparatus, Barcelona, Spain) and recorded the average (3 trials) maximum speed reached before falling off the rod. On the same day, rats were placed in the center of an open-field arena (50x50 cm) for 20 min and locomotion was video-tracked (ViewPoint, Civrieux, France) and quantified.

Statistical analysis

Statistical analysis was performed using Prism 8 (GraphPad Software, San Diego, CA, USA). Comparisons between two experimental groups were performed using a non-parametric Mann-Whitney test unless otherwise mentioned. RABV input distribution in space were analyzed with 2-way ANOVA test with Tukey's correction for multiple comparisons. SWD power follow-up in time was analyzed with 2-way ANOVA with Sidak's correction. All data in Figures are presented as box-and-whisker plots showing interquartile interval, median, maximum, minimum, and mean values unless otherwise mentioned. Statistical details are provided in Supplementary Table 2. The significance level for all statistical analysis was set at $p \leq 0.05$.

Data availability

The datasets generated during the current study are available from the corresponding authors upon reasonable request.

Results

Increased presynaptic connectivity of wS1 cortical neurons in GAERS rats

We hypothesized that SWD generation in absence epilepsy could result from aberrant wS1 neuron connectivity that could facilitate neuronal hypersynchronization observed during seizures. To test this hypothesis, we aimed at dissecting the structural connectivity of wS1 neurons in adult GAERS compared to control non-epileptic rats. To identify brain-wide synaptic partners projecting onto wS1 neurons, we used rabies virus (RABV)-mediated retrograde monosynaptic tracing of connections (Fig. 1A) [29]. GAERS and control rats were injected in the upper or deeper layers of wS1 with a lentivirus encoding the TVA receptor for the EnvA-pseudotyped RABV and the RABV glycoprotein G together with a histone-GFP reporter. Two weeks later, TVA-expressing cortical neurons were selectively transduced with the EnvA-pseudotyped, G-deleted RABV that encoded mCherry and subsequently spread transsynaptically from GFP/mCherry-double positive neurons (i.e. so-called starter neurons) to their first-order presynaptic partners that then expressed mCherry only (Fig. 1A). We quantified the numbers of starter neurons and presynaptic neurons at 7 days post RABV injection [29,30].

In a first set of experiments, animals were injected with the lentivirus and RABV in L2/3 upper cortical layers (Fig. 1B, C and Supplementary Fig. 1A, B). Strikingly, L2/3 GFP/mCherry+ starter neurons in GAERS displayed a strong and significant increase in the total number of mCherry+ presynaptic partners compared to control rats (about 3-fold; Mann-Whitney test, $p \leq 0.01$; Fig. 1B, C and E). We next examined the distribution of mCherry+ presynaptic neurons among all cortical layers in wS1. Inputs arising from presynaptic partners located in L2/3 were significantly increased in GAERS compared to controls (2-way ANOVA, Tukey post-hoc correction, $p \leq 0.01$; Fig. 1B, C and F). We also observed a significant increase in mCherry+ presynaptic neurons located in L5/6 (2-way ANOVA, Tukey post-hoc correction, $p \leq 0.01$; Fig. 1B, C and F). Next, to more precisely determine the spatial location of wS1 presynaptic partners along the rostro-caudal axis, we quantified their numbers within successive 80-µm bins spreading from the starter cell area (Fig. 1G). Overall, we observed in both GAERS and control rats that the vast majority of presynaptic partners in all cortical layers was located in the close antero-posterior vicinity of L2/3 starter neurons (Fig. 1H). Interestingly, this distance-based quantification also revealed a significantly increased number of presynaptic partners in L4 in GAERS in the close antero-posterior vicinity of starter neurons ($p \leq 0.05$, Fig. 1H and I), while this increase did not reach significance when considering the entire rostro-caudal extent of L4 (Fig. 1F).

In the next set of experiments, injections of lentivirus and RABV were restricted to L5/6 deep cortical layers (Fig. 2A, B and Supplementary Fig. 1A, C). As observed for L2/3 starter neurons, L5/6 starter cells displayed a strong and significant increase in the total number of mCherry+ presynaptic partners in GAERS compared to controls (about 3-fold; Mann-Whitney test, $p \leq 0.01$; Fig. 2A, B and D). Regarding distribution of presynaptic neurons among wS1 cortical layers, inputs onto L5/6 starter neurons mostly originated from L5/6 presynaptic partners in both control and GAERS rats (Fig. 2A, B, E and G). We found, however, a significant increase in L5/6 intralaminar inputs in GAERS compared to controls (2-way ANOVA, Tukey post-hoc correction, $p \leq 0.0001$; Fig. 2E). Next, we analyzed the spatial distribution of these inputs along the antero-posterior axis and quantified their numbers within successive 80-µm bins spreading from the starter cell area (Fig. 2F). These quantifications revealed that increased presynaptic partners in L5/6 cortical layers were distributed over a significantly larger area in GAERS compared to controls (2-way ANOVA, Tukey post-hoc correction, $p \leq 0.05$; Fig. 2G and H). In addition, this analysis revealed a significantly increased number of presynaptic partners in L4 in GAERS in the close antero-posterior vicinity of starter neurons (2-way ANOVA, Tukey post-hoc correction, $p \leq 0.05$; Fig. 2H).

We then examined long-range synaptic inputs originating from remote brain regions and innervating wS1 starter neurons in GAERS and non-epileptic animals (Supplementary Fig. 1D). We found relatively few long-range projection neurons innervating L2/3 starter cells in both strains (Supplementary Fig. 1E). We observed in both GAERS and controls that mCherry+ presynaptic neurons projecting onto L5/6 starter cells were located in the thalamus, motor cortices, secondary somatosensory cortex and other areas of the S1 cortex (i.e., S1 body). Of note, innervation of L5/6 starter neurons by S1 body presynaptic partners was significantly increased in GAERS compared to controls (Supplementary Fig. 1F, 2-way ANOVA, Tukey post-hoc correction, $p \leq 0.001$).

Taken together, our data evidence that wS1 neurons in L2/3 and L5/6 layers in GAERS receive significantly more synaptic inputs that not only originate from the respective L2/3 and L5/6 cortical layers (i.e. intralaminar connections), but also from other wS1 cortical layers.

wS1 neurons receive increased GABAergic innervation in GAERS rats

Because inhibitory neurotransmission plays a critical role in the shaping, triggering and synchronization of cortical activity [43], we next examined synaptic inputs from GABAergic neurons onto starter neurons in the same groups of GAERS and non-epileptic animals (Fig. 3). In control rats, GABA+/mCherry+ presynaptic partners projecting onto L2/3 starter cells were mainly located within L2/3, with only very few GABA innervation from L5/6 (Fig. 3A and B), in agreement with previous studies [44]. To our surprise, we evidenced in GAERS that L2/3 starter cells received a significantly increased number of GABAergic inputs from L5/6 compared to controls (Fig. 3B, 2-way ANOVA, Tukey post-hoc correction, $p \leq 0.05$), alongside a moderate increase in GABAergic innervation from L2/3 and L4. We next observed that GABAergic synaptic inputs onto L5/6 starter neurons mainly originated from inhibitory neurons located within the same cortical L5/6 layers in both GAERS and non-epileptic rats (Fig. 3C). Strikingly, however, GABAergic innervation from L5/6 interneurons was significantly increased in GAERS (Fig. 3C, 2-way ANOVA, Tukey post-hoc correction, $p \leq 0.01$). Taken together, our data reveal that L2/3 and L5/6 neurons receive increased innervation by GABAergic neurons located in deep L5/6 cortical layers in GAERS animals.

Disruption of aberrant wS1 neuronal networks in GAERS by X-ray-mediated microtransections

The finding that wS1 neurons in GAERS showed increased connectivity prompted us to investigate whether this aberrant connectivity pattern contributes to wS1 neuron hypersynchronization leading to seizures. To address this question, we first sought to identify how to disrupt this overall aberrant connectivity in order to subsequently be able to study its role. We examined whether synchrotron-generated X-ray microtransections, that were previously shown to reduce seizures in GAERS [32,33], could globally disrupt the increased connectivity to wS1 neurons, i.e. including both local connections and long-range projections . Synchrotron-generated X-ray microbeams, with limited divergence of the energy and excellent tissue tolerance [35] were shown to provide an innovative radiosurgical procedure that allows precise transection of a given brain region. Eleven vertical microtransections were performed using 50 µm-thick parallel microbeams (spaced from 400 µm) in the left wS1 cortex of GAERS rats (Fig. 4A). In agreement with previous studies [45,33], synchrotron-generated microbeams induced a discrete and selective loss of NeuN+ neurons along the beam paths through all cortical layers, as revealed by immunohistological analysis at two months post irradiation (Fig. 4A and B). Importantly, however, no sign of neuronal degeneration could be detected outside the microbeam tracks in the surrounding cortical tissue at two months after irradiation, thus indicating that X-ray-generated microbeams induced sharp microtransections within the cortical tissue (Fig. 4A and B). Of note, the microvasculature revealed by Rat Endothelial Cells Antibody (RECA) immunostaining was preserved both inside and outside the transection tracks (Fig. 4B), in line with previous report [35]. In addition, only a few GFAP+ astrocytes were detected within the transections paths or at the edges of the microbeam tracks (Fig. 4C) and no increase in Iba1+ microglia could be observed (Fig. 4D).

Next, we examined whether synchrotron-generated microtransections disrupted the connectivity of wS1 neurons. To this end, we followed the same RABV-mediated strategy as described above and injected synchrotron-irradiated GAERS (GAERS-SI) with successively the lentivirus encoding TVA and glycoprotein G (GFP) and the RABV (mCherry) in L2/3 or L5/6. At 6 to 8 weeks post irradiation, connectivity ratios in GAERS-SI were compared to GAERS and non-epileptic control rats. We observed a marked and significant reduction in the total number of presynaptic inputs projecting to L5/6 starter neurons in GAERS-SI when compared to GAERS (Fig. 2D, Mann-Whitney test, $p \leq 0.05$). Importantly, no overt differences in the connectivity ratios of L5/6 neurons (Fig. 2 D and E) and the spatial distribution of presynaptic inputs (Supplementary Fig. 1 I,J) could be observed between non-epileptic control and GAERS-SI rats. Our detailed quantifications revealed that the overall reduction of presynaptic connectivity in GAERS-SI was mainly due to a significant decrease of L5/6 intralaminar presynaptic inputs compared to GAERS (Fig. 2E, 2-way ANOVA, Tukey post-hoc correction, $p \leq 0.0001$). In addition, the analysis of presynaptic input distribution along the rostro-caudal axis confirmed a significant decrease in the number of inputs originating from L5/6 but also from L4 in GAERS-SI compared to GAERS (Fig. 2I and J, 2-way ANOVA, Tukey post-hoc correction, $p \leq 0.05$). In particular, we also found a significant decrease of L5/6 intralaminar GABAergic inputs to L5/6 starter neurons in GAERS-SI compared to GAERS, and GABAergic innervation in GAERS-SI was similar to control animals (Fig. 3C, 2-way ANOVA, Tukey post-hoc correction, $p \leq 0.01$). While cortical microtransections did not seem to affect significantly the long-range connectivity projecting onto wS1 starter neurons (Supplementary Fig. 1E, F), a trend towards a decreased thalamic input to L5/6 starter neurons was observed (Supplementary Fig. 1F, 2-way ANOVA, Tukey post-hoc correction, $p=0.74$). To our surprise, we observed that the total number of presynaptic inputs projecting to L2/3 starter neurons was not severely affected in GAERS-SI compared to GAERS (Fig. 1E) and remained significantly different from non-epileptic control animals (Fig. 1E and Supplementary Fig. 1G and H). Nevertheless, intralaminar innervation by L2/3 presynaptic partners was significantly decreased in GAERS-SI compared to GAERS when considering inputs in the close antero-posterior vicinity of L2/3 starter neurons (Fig. 1J and K, 2-way ANOVA, Tukey post-hoc correction, $p \leq 0.05$).

Taken together, these data show that synchrotron-generated microtransections applied within wS1 disrupt overall aberrant wS1 neuronal networks observed in GAERS and, in particular, are most effective in suppressing the aberrantly increased intralaminar connectivity to L5/6 neurons.

Disrupting aberrant connectivity of wS1 neurons in GAERS reduces wS1 neuron synchronization

Next, we studied whether the increased wS1 neuron connectivity that we evidenced in GAERS (Fig. 1 and Fig. 2) contributes to increased synchronization of wS1 neurons leading to seizures. To this end, we examined whether synchrotron-mediated disruption of wS1 neuron hyperconnectivity affects neuronal synchronization. In a first set of experiments, we performed in vivo recordings of local field potentials (LFPs) in wS1 in freely moving GAERS and GAERS-SI from 2 to 8 weeks post irradiation. In line with our previous reports [32,33], we confirmed that ipsilateral microtransections within wS1 were followed by drastic decrease of SWD amplitude in GAERS-SI compared to GAERS (Fig. 5A). Time-frequency analysis revealed a significant decrease in SWD power in GAERS-SI compared to GAERS (Fig. 5A), as soon as 2 weeks post irradiation and for up to 2 months (Fig. 5B, 2-way ANOVA, $p \leq 0.05$), which is indicative of decreased neuronal synchronization [46]. Yet, neither the internal frequency of SWDs (Fig. 5A, arrows) nor SWD occurrence were modified (Supplementary Fig. 2 A, B and C), in line with previous reports showing that only bilateral manipulations suppressed SWDs [33].

Next, we analyzed the waveform of the spike component recorded during SWDs (Fig. 5C), that is known to reflect neuronal synchronization [47,19]. Indeed, the magnitude and shape of extracellular field potential recordings depend on the distance to the source and the number of neurons involved as well as the temporal synchronization of their activity [46]. In GAERS, wS1 pyramidal neurons are active only during the spike component of SWDs and silent during the wave [17,47]. Moreover, the synchronization of cortical neurons shapes the epileptic spike. Indeed, the progressive development of the epileptic spike during epileptogenesis, i.e. increased slope and amplitude, Has been shown to be characterized by an increase of the synchronization of pyramidal neurons [19]. The positive slope of the spikes (Fig. 5C) was significantly decreased in GAERS-SI compared to GAERS at 2, 4 and 8 weeks after irradiation (Fig. 5D, E and F, Mann-Whitney test, $p \leq 0.05$), thus reflecting a stable decrease in wS1 neuron synchronization compared to GAERS. Furthermore, we observed that the negative slope of the spikes was significantly decreased at 2 weeks post irradiation (Fig. 5D). These bidirectional changes also reflect ongoing modifications of wS1 neuron synchronization properties. No overt modifications in the spike duration could be detected after microtransections (Fig. 5D, E and F, Mann-Whitney test), in line with maintenance of the internal frequency of SWD in GAERS-SI (Fig. 5A, arrowheads).

In a next set of experiments, to further examine whether increased structural connectivity of wS1 neurons in GAERS affects the pathological neuronal synchronization associated with SWD initiation, we followed an alternative approach and performed *in vivo* recordings across wS1 neuronal layers using multi-channel silicon probes in sedated and immobilized GAERS and GAERS-SI at 4-8 weeks after synchrotron-mediated microtransections (Fig. 6A). We performed current source density analysis, which reflects the direction of extracellular ion changes and that can be used to estimate neuronal activity [46]. During the first spike of SWD in GAERS, this analysis revealed an important activity in L5/6 that shifted thereafter toward L2/3 and finally to L4 (Fig. 6B, left). These data confirmed the sequence of propagation of the paroxysmal activity from L5/6 to L2/3 and L4 during SWDs, as we have previously suggested [17]. In sharp contrast, this analysis revealed in GAERS-SI a decreased activity in L5/6 followed by a more prominent activity in L2/3 and L4 compared to GAERS (Fig. 6B, right). This reduction of neuronal activity in L5/6 suggests a decreased neuronal synchronization in GAERS-SI, resulting from microtransection-mediated disruption of wS1 neuron hyperconnectivity.

Next, to further confirm this decreased neuronal synchronization during SWDs after synchrotron-generated microtransections, we examined neuronal activity by multi-unit activity analysis among wS1 layers (Fig. 6C). Neuronal activity was significantly increased in L4 both during SWDs and interictal periods (i.e., between SWDs) in GAERS-SI when compared to GAERS (Fig. 6D and E, Mann-Whitney test, $p \leq 0.05$). To determine whether this increased L4 activity was associated with modified timing of neuronal firing and synchronization, we examined the probability of neuronal firing during the spike component of SWDs. In GAERS, the discharge probability followed a Gaussian distribution in L2/3, L4 and L5/6 (Fig. 6F, upper panels). In contrast, values in GAERS-SI in all layers did not fit to the Gaussian distribution as in GAERS (Fig. 6F, lower panels; L2/3: $R^2=0.96$ *vs* 0.77; L4: $R^2=0.90$ *vs* 0.85; L5/6, $R^2=0.92$ *vs* 0.78, in GAERS and GAERS-SI, respectively). In addition, the latency between the peak of neuronal discharges and the epileptic spike was significantly increased in L5/6 neurons in GAERS-SI (Fig. 6I, Mann-Whitney test, $p \leq 0.01$), thus indicating earlier activation of these neurons. Finally, neurons in all layers displayed a broader distribution of activity overtime in GAERS-SI than in GAERS (Fig. 6F and Supplementary Fig. 3B), thus confirming decreased synchronization of neuronal activity in GAERS-SI.

Finally, LFP recordings did not reveal overt differences in spectral activity between GAERS and GAERS-SI between seizures (i.e., interictal; Supplementary Fig. 2D), thus suggesting no deleterious effects of microtransections on physiological processing. In addition, we did not observe any side effect on the general behavior of GAERS-SI rats 2 months after synchrotron-generated microtransections. In particular, no alterations of locomotion and sensorimotor coordination were observed when compared to non-transected GAERS (Supplementary Fig. 4A and B). Air puff-generated, somatosensory-evoked potentials were unaltered in GAERS-SI (Supplementary Fig. 4C, D, E and F). These results confirmed that unilateral synchrotron-induced microtransections within wS1 did not induce ischemic, inflammatory, behavioral or sensory side-effects, in agreement with previous studies [35,32,33,48].

Taken together, these results show that disrupting the increased structural connectivity of wS1 neurons observed in GAERS by synchrotron-generated microtransections resulted in decreased synchronized activation of wS1 neurons and seizures. Thus, these data indicate that the increased anatomical connectivity of wS1 neurons in GAERS plays a critical role in synchronizing neuronal activation leading to seizures. In addition, our results support a critical role of deep layer neuron connections in the control of neuronal activation and pathological synchronization within L5/6, which in turn can affect L4 and L2/3 neuronal activity.

Discussion

Using RABV-mediated retrograde synaptic tracing, our study demonstrates for the first time the existence of an increased structural neuronal connectivity within the wS1 cortex that was previously shown to be the area of SWDs initiation in GAERS, a well-recognized model of absence epilepsy [28]. Indeed, we found in GAERS that cortical neurons located in both upper and deeper layers of wS1 displayed aberrant and significantly increased input connections, including enhanced innervation by GABAergic interneurons in L5/6. The disruption of these aberrant wS1 connections by synchrotron-generated X-ray microtransections led to a significant reduction of SWD power and a more diffuse or less time-constrained neuronal activity during the spikes of SWDs. Both data are indicative of a decreased neuronal synchronization during seizures after wS1 microtransection. Therefore, our study shows that an increased connectivity of wS1 neurons in GAERS is critical for the pathological neuronal synchronization of ictogenic neurons.

Using genetic models of absence epilepsy in rats, we and others have shown that the S1 is critical in the initiation of SWDs [15,17,49,50]. Here, using multi-site silicon probes across the different cortical layers and current source density analysis, we confirmed the vertical L5/6→L2/3→L4 sequence of events between layers during spike-and-wave initiation, which is the opposite of the canonical sensory sequence [8]. We recently showed that GAERS are, however, as performant as non-epileptic rats in texture discrimination task [27]. The increased connectivity of upper and deep layer neurons observed in the present study may therefore not affect the sensory functions of wS1. This is confirmed by the absence of difference in the electrophysiological response evoked in wS1 by air puff stimulation in GAERS-SI. Our data therefore suggest the existence of a neuronal circuit that carries properties favoring seizures while allowing normal sensory processing within wS1 in GAERS. Whether these two circuits involve the same neuronal population, or neurons that are specialized in one or the other circuit, remains to be addressed.

L5/6 neurons integrate information through excitatory connections from L2/3 of the same column [51] as well as from L2/3, L5 and L6A of adjacent columns, also called “horizontal” connections [52]. RABV-mediated tracing evidenced an increased connectivity in GAERS with an increased number of presynaptic partners that extend horizontally over several hundreds of micrometers from L5/6 starter neurons in the rostro-caudal axis, whereas increased L2/3 connections mainly spread within the dorso-ventral axis of the cortical column. This difference could explain why L5/6 connections were mostly disrupted by synchrotron-generated microtransections which are orthogonal to the surface of the brain. Hence, we propose that horizontal connections between deep layer neurons in GAERS are critical players in the pathological neuronal synchronization of ictogenic neurons. Furthermore, we demonstrated recently that this pathological neuronal synchronization is progressively acquired during cortical maturation in GAERS [19]. Our present results also suggest that the increased number of synaptic inputs projecting onto L5/6 neurons could also increase incoming information to these neurons (during and in between SWDs), thereby explaining their hyperexcitable state, as previously evidenced by intracellular *in vivo* recordings [17]. Our data therefore support the notion that the hyperactivity of ictogenic neurons in absence epilepsy is determined by the development of increased connectivity within pro-ictogenic neuronal networks that could take place during cortical maturation. Future studies will be required to explore in more detail the specific role of the increased input from the distinct labeled presynaptic partners, including a potential role of the thalamic input, on the pathological synchronization of wS1 ictogenic neurons.

Inhibition in the sensory cortex is known to be mostly local [44] and to control excitatory cells [9,53,54]. In particular, GABAergic neurons actively modulate cortical functions by filtering information [55] and modulating its propagation [56]. Our RABV tracing results revealed that, in GAERS, a significant proportion of increased synaptic inputs to L2/3 and L5/6 neurons originate from L5/6 GABAergic neurons. This, together with the increase of cortical GABAergic neurons observed in GAERS [27], supports the hypothesis that inhibition in wS1 could constrain over time the activation of excitatory cells [43], and therefore facilitate their synchronization during SWDs. Indeed, after synchrotron-generated X-ray microtransections, we observed a drastic reduction of GABAergic inputs to L2/3 and L5/6 wS1 neurons associated with reduction of neuronal synchronization and seizure power. Thus, it is tempting to speculate that GABAergic inhibition could play a critical role in the neuronal synchronization leading to SWD generation in GAERS. Finally, the inhibitory connections from L5/6 GABAergic neurons to L2/3 neurons may allow a progressive time locking that would favor the entrainment of L2/3 neurons by the paroxysmal activity initiated in L5/6 pyramidal neurons and could consequently shape the spike and the wave components of SWDs [43]. This hypothesis is supported by the inhibitory feedback onto pyramidal cells during the wave component of SWDs, as suggested in GAERS [57]. Further experiments to identify the precise contribution of potential subpopulations of GABAergic interneurons and to determine whether they contribute to the increased tonic inhibition observed in GAERS and other models of absence epilepsy [58] will be necessary to decipher the mechanisms of SWD initiation.

In conclusion, our results demonstrate that cortical wS1 neurons located in both deep and superficial layers in GAERS display aberrant and significantly increased connectivity. Our study provides evidence that this increased structural connectivity represents a critical pathological substrate for increased synchronization of ictogenic neurons and generation of absence seizures.

Acknowledgements:

We thank E Brun and O David for their help on signal and image analysis as well as I Guillemain, S Charpier and E Fino for their helpful comments on the manuscript. We thank C Massera for her excellent technical support for the production of lentiviral particles.

Funding:

This work was supported by funding from the Institut National de la Santé et de la Recherche Médicale (INSERM) and the following grants: Agence National de la Recherche (ANR, EPIRAD, ANR-13-BSV1-0012-01 2013 and SoAbsence, ANR-16-CE37-0021 2016) to A.D.; Agence Nationale de la Recherche (ANR, ReprogramEpi, ANR-14-CE13-0001), LabEx CORTEX (ANR-11-LABX-0042 of Lyon University within the program "Investissements d'Avenir" ANR-11-IDEX-0007), Fédération pour la Recherche sur le Cerveau (FRC), Fondation Française pour la Recherche sur l'Epilepsie (FFRE), and Citizens United for Research in Epilepsy (CURE, Award ID: 262178) to C.H.. FS received support from the Ligue Française contre l'Epilepsie and Grenoble Alpes University.

Competing interests:

The authors declare no competing interests.

Supplementary material:

Supplementary material is available at *Brain* online.

References:

1. DeNardo LA, Berns DS, DeLoach K, Luo L. Connectivity of mouse somatosensory and prefrontal cortex examined with trans-synaptic tracing. *Nat Neurosci*. 2015;18(11):1687-1697. doi:10.1038/nn.4131

2. Narayanan RT, Egger R, Johnson AS, et al. Beyond Columnar Organization: Cell Type- and Target Layer-Specific Principles of Horizontal Axon Projection Patterns in Rat Vibrissal Cortex. *Cereb Cortex N Y N 1991*. 2015;25(11):4450-4468. doi:10.1093/cercor/bhv053

3. Bureau I, Shepherd GM, Svoboda K. Precise development of functional and anatomical columns in the neocortex. *Neuron*. 2004;42(5):789-801.

4. Shepherd GMG, Stepanyants A, Bureau I, Chklovskii D, Svoboda K. Geometric and functional organization of cortical circuits. *Nat Neurosci*. 2005;8(6):782-790. doi:10.1038/nn1447

5. van der Bourg A, Yang J-W, Reyes-Puerta V, et al. Layer-Specific Refinement of Sensory Coding in Developing Mouse Barrel Cortex. *Cereb Cortex*. Published online September 12, 2016. doi:10.1093/cercor/bhw280

6. Harris KD, Mrsic-Flogel TD. Cortical connectivity and sensory coding. *Nature*. 2013;503(7474):51-58. doi:10.1038/nature12654

7. Douglas RJ, Martin KAC, Whitteridge D. A Canonical Microcircuit for Neocortex. *Neural Comput*. 1989;1(4):480-488. doi:10.1162/neco.1989.1.4.480

8. Lübke J, Feldmeyer D. Excitatory signal flow and connectivity in a cortical column: focus on barrel cortex. *Brain Struct Funct*. 2007;212(1):3-17. doi:10.1007/s00429-007-0144-2

9. Wilent WB, Contreras D. Dynamics of excitation and inhibition underlying stimulus selectivity in rat somatosensory cortex. *Nat Neurosci*. 2005;8(10):1364-1370. doi:10.1038/nn1545

10. Feldt Muldoon S, Soltesz I, Cossart R. Spatially clustered neuronal assemblies comprise the microstructure of synchrony in chronically epileptic networks. *Proc Natl Acad Sci*. 2013;110(9):3567-3572. doi:10.1073/pnas.1216958110

11. Yan B, Li P. The emergence of abnormal hypersynchronization in the anatomical structural network of human brain. *NeuroImage*. 2013;65(Supplement C):34-51. doi:10.1016/j.neuroimage.2012.09.031

12. Althaus AL, Zhang H, Parent JM. Axonal plasticity of age-defined dentate granule cells in a rat model of mesial temporal lobe epilepsy. *Neurobiol Dis*. 2016;86:187-196. doi:10.1016/j.nbd.2015.11.024

13. Uhlhaas PJ, Singer W. Neural Synchrony in Brain Disorders: Relevance for Cognitive Dysfunctions and Pathophysiology. *Neuron*. 2006;52(1):155-168. doi:10.1016/j.neuron.2006.09.020

14. Loiseau P, Duche B, Pédespan J-M. Absence epilepsies. *Epilepsia*. 1995;36(12):1182-1186.

15. Meeren HKM, Pijn JPM, Van Luijtelaar ELJM, Coenen AML, Lopes da Silva FH. Cortical focus drives widespread corticothalamic networks during spontaneous absence seizures in rats. *J Neurosci Off J Soc Neurosci*. 2002;22(4):1480-1495.

16. Holmes MD, Brown M, Tucker DM. Are “Generalized” Seizures Truly Generalized? Evidence of Localized Mesial Frontal and Frontopolar Discharges in Absence. *Epilepsia*. 2004;45(12):1568-1579. doi:10.1111/j.0013-9580.2004.23204.x

17. Polack P-O, Guillemain I, Hu E, Deransart C, Depaulis A, Charpier S. Deep Layer Somatosensory Cortical Neurons Initiate Spike-and-Wave Discharges in a Genetic Model of Absence Seizures. *J Neurosci*. 2007;27(24):6590-6599. doi:10.1523/JNEUROSCI.0753-07.2007

18. Tucker DM, Brown M, Luu P, Holmes MD. Discharges in ventromedial frontal cortex during absence spells. *Epilepsy Behav*. 2007;11(4):546-557. doi:10.1016/j.yebeh.2007.04.023

19. Jarre G, Altwegg-Boussac T, Williams MS, et al. Building Up Absence Seizures in the Somatosensory Cortex: From Network to Cellular Epileptogenic Processes. *Cereb Cortex*. 2017;27(9):4607-4623. doi:10.1093/cercor/bhx174

20. Danober L, Deransart C, Depaulis A, Vergnes M, Marescaux C. Pathophysiological mechanisms of genetic absence epilepsy in the rat. *Prog Neurobiol*. 1998;55(1):27-57.

21. Depaulis A, David O, Charpier S. The genetic absence epilepsy rat from Strasbourg as a model to decipher the neuronal and network mechanisms of generalized idiopathic epilepsies. *J Neurosci Methods*. 2016;260:159-174. doi:10.1016/j.jneumeth.2015.05.022

22. Crunelli V, Lőrincz ML, McCafferty C, et al. Clinical and experimental insight into pathophysiology, comorbidity and therapy of absence seizures. *Brain*. 2020;143(8):2341-2368. doi:10.1093/brain/awaa072

23. Powell KL, Cain SM, Ng C, et al. A Cav3.2 T-Type Calcium Channel Point Mutation Has Splice-Variant-Specific Effects on Function and Segregates with Seizure Expression in a Polygenic Rat Model of Absence Epilepsy. *J Neurosci*. 2009;29(2):371-380. doi:10.1523/JNEUROSCI.5295-08.2009

24. Yalçın Ö. Genes and molecular mechanisms involved in the epileptogenesis of idiopathic absence epilepsies. *Seizure*. 2012;21(2):79-86. doi:10.1016/j.seizure.2011.12.002

25. Chen Y, Lu J, Pan H, et al. Association between genetic variation of CACNA1H and childhood absence epilepsy. *Ann Neurol*. 2003;54(2):239-243. doi:10.1002/ana.10607

26. Khosravani H, Altier C, Simms B, et al. Gating Effects of Mutations in the Cav3.2 T-type Calcium Channel Associated with Childhood Absence Epilepsy *. *J Biol Chem*. 2004;279(11):9681-9684. doi:10.1074/jbc.C400006200

27. Studer F, Laghouati E, Jarre G, David O, Pouyatos B, Depaulis A. Sensory coding is impaired in rat absence epilepsy. *J Physiol*. 2019;597(3):951-966. doi:10.1113/JP277297

28. Depaulis A, Charpier S. Pathophysiology of absence epilepsy: Insights from genetic models. *Neurosci Lett*. 2018;667:53-65. doi:10.1016/j.neulet.2017.02.035

29. Wickersham IR, Lyon DC, Barnard RJO, et al. Monosynaptic Restriction of Transsynaptic Tracing from Single, Genetically Targeted Neurons. *Neuron*. 2007;53(5):639-647. doi:10.1016/j.neuron.2007.01.033

30. Miyamichi K, Amat F, Moussavi F, et al. Cortical representations of olfactory input by trans-synaptic tracing. *Nature*. 2011;472(7342):191-196. doi:10.1038/nature09714

31. Bergami M, Masserdotti G, Temprana SG, et al. A Critical Period for Experience-Dependent Remodeling of Adult-Born Neuron Connectivity. *Neuron*. 2015;85(4):710-717. doi:10.1016/j.neuron.2015.01.001

32. Pouyatos B, Serduc R, Chipaux M, et al. Synchrotron X-ray interlaced microbeams suppress paroxysmal oscillations in neuronal networks initiating generalized epilepsy. *Neurobiol Dis*. 2013;51:152-160. doi:10.1016/j.nbd.2012.11.005

33. Pouyatos B, Nemoz C, Chabrol T, et al. Synchrotron X-ray microtransections: a non invasive approach for epileptic seizures arising from eloquent cortical areas. *Sci Rep*. 2016;6:27250. doi:10.1038/srep27250

34. Callaway EM, Luo L. Monosynaptic Circuit Tracing with Glycoprotein-Deleted Rabies Viruses. *J Neurosci Off J Soc Neurosci*. 2015;35(24):8979-8985. doi:10.1523/JNEUROSCI.0409-15.2015

35. Serduc R, Bräuer-Krisch E, Siegbahn EA, et al. High-Precision Radiosurgical Dose Delivery by Interlaced Microbeam Arrays of High-Flux Low-Energy Synchrotron X-Rays. *PLOS ONE*. 2010;5(2):e9028. doi:10.1371/journal.pone.0009028

36. Nemoz C, Kibleur A, Hyacinthe JN, et al. In vivo pink-beam imaging and fast alignment procedure for rat brain tumor radiation therapy. *J Synchrotron Radiat*. 2016;23(1):339-343. doi:10.1107/S1600577515018561

37. Serduc R, Bouchet A, Pouyatos B, et al. Synchrotron X Ray Induced Axonal Transections in the Brain of Rats Assessed by High-Field Diffusion Tensor Imaging Tractography. *PLOS ONE*. 2014;9(2):e88244. doi:10.1371/journal.pone.0088244

38. Paxinos G, Watson C. The Rat Brain in Stereotaxic Coordinates - 6th Edition. Published 2007. Accessed November 22, 2017. https://www.elsevier.com/books/the-rat-brain-in-stereotaxic-coordinates/paxinos/978-0-12-374121-9

39. Kandel A, Buzsáki G. Cellular–synaptic generation of sleep spindles, spike-and-wave discharges, and evoked thalamocortical responses in the neocortex of the rat. *J Neurosci*. 1997;17(17):6783-6797.

40. Mahon S, Charpier S. Bidirectional plasticity of intrinsic excitability controls sensory inputs efficiency in layer 5 barrel cortex neurons in vivo. *J Neurosci Off J Soc Neurosci*. 2012;32(33):11377-11389. doi:10.1523/JNEUROSCI.0415-12.2012

41. Chipaux M, Vercueil L, Kaminska A, Mahon S, Charpier S. Persistence of Cortical Sensory Processing during Absence Seizures in Human and an Animal Model: Evidence from EEG and Intracellular Recordings. *PLOS ONE*. 2013;8(3):e58180. doi:10.1371/journal.pone.0058180

42. Nicholson C, Freeman JA. Theory of current source-density analysis and determination of conductivity tensor for anuran cerebellum. *J Neurophysiol*. 1975;38(2):356-368. doi:10.1152/jn.1975.38.2.356

43. Isaacson JS, Scanziani M. How Inhibition Shapes Cortical Activity. *Neuron*. 2011;72(2):231-243. doi:10.1016/j.neuron.2011.09.027

44. Fino E, Yuste R. Dense inhibitory connectivity in neocortex. *Neuron*. 2011;69(6):1188-1203. doi:10.1016/j.neuron.2011.02.025

45. Studer F, Serduc R, Pouyatos B, et al. Synchrotron X-ray microbeams: A promising tool for drug-resistant epilepsy treatment. *Phys Med*. 2015;31(6):607-614. doi:10.1016/j.ejmp.2015.04.005

46. Buzsáki G, Anastassiou CA, Koch C. The origin of extracellular fields and currents--EEG, ECoG, LFP and spikes. *Nat Rev Neurosci*. 2012;13(6):407-420. doi:10.1038/nrn3241

47. Williams MS, Altwegg-Boussac T, Chavez M, Lecas S, Mahon S, Charpier S. Integrative properties and transfer function of cortical neurons initiating absence seizures in a rat genetic model: Epileptic seizures and information processing. *J Physiol*. Published online August 2016. doi:10.1113/JP272162

48. Fardone E, Bravin A, Conti A, et al. Rat sensorimotor cortex tolerance to parallel transections induced by synchrotron-generated X-ray microbeams. *Sci Rep*. 2017;7(1):14290. doi:10.1038/s41598-017-14757-3

49. David O, Guillemain I, Saillet S, et al. Identifying Neural Drivers with Functional MRI: An Electrophysiological Validation. Valdes-Sosa P, ed. *PLoS Biol*. 2008;6(12):e315. doi:10.1371/journal.pbio.0060315

50. Polack P-O, Mahon S, Chavez M, Charpier S. Inactivation of the Somatosensory Cortex Prevents Paroxysmal Oscillations in Cortical and Related Thalamic Neurons in a Genetic Model of Absence Epilepsy. *Cereb Cortex*. 2009;19(9):2078-2091. doi:10.1093/cercor/bhn237

51. Lefort S, Tomm C, Floyd Sarria J-C, Petersen CCH. The Excitatory Neuronal Network of the C2 Barrel Column in Mouse Primary Somatosensory Cortex. *Neuron*. 2009;61(2):301-316. doi:10.1016/j.neuron.2008.12.020

52. Schnepel P, Kumar A, Zohar M, Aertsen A, Boucsein C. Physiology and Impact of Horizontal Connections in Rat Neocortex. *Cereb Cortex*. 2015;25(10):3818-3835. doi:10.1093/cercor/bhu265

53. Cruikshank SJ, Lewis TJ, Connors BW. Synaptic basis for intense thalamocortical activation of feedforward inhibitory cells in neocortex. *Nat Neurosci*. 2007;10(4):462-468. doi:10.1038/nn1861

54. Silberberg G, Markram H. Disynaptic Inhibition between Neocortical Pyramidal Cells Mediated by Martinotti Cells. *Neuron*. 2007;53(5):735-746. doi:10.1016/j.neuron.2007.02.012

55. Yu J, Gutnisky DA, Hires SA, Svoboda K. Layer 4 fast-spiking interneurons filter thalamocortical signals during active somatosensation. *Nat Neurosci*. 2016;19(12):1647-1657. doi:10.1038/nn.4412

56. Petersen CCH, Hahn TTG, Mehta M, Grinvald A, Sakmann B. Interaction of sensory responses with spontaneous depolarization in layer 2/3 barrel cortex. *Proc Natl Acad Sci*. 2003;100(23):13638-13643. doi:10.1073/pnas.2235811100

57. Chipaux M, Charpier S, Polack P-O. Chloride-mediated inhibition of the ictogenic neurones initiating genetically-determined absence seizures. *Neuroscience*. 2011;192:642-651. doi:10.1016/j.neuroscience.2011.06.037

58. Cope DW, Giovanni GD, Fyson SJ, et al. Enhanced tonic $GABA_A$ inhibition in typical absence epilepsy. *Nat Med*. 2009;15(12):1392. doi:10.1038/nm.2058

Figure legends

Figure 1: RABV monosynaptic retrograde tracing of L2/3 neuronal connectivity in wS1. **(A)** Experimental procedure for tracing monosynaptic inputs to wS1 by injection of G-TVA expressing lentivirus followed by RABV. **(B-D)** Right: Examples of coronal sections showing starter cell zone in L2/3 with lentivirus-only infected cells (green), starter cells (yellow) and their first-order presynaptic partners (red). Left: Insets in starter cell zone with arrowheads pointing to starter cells. Scale bars: 200 µm (main panels) and 50 µm (inset). For Control (B),

GAERS (C) and synchrotron-irradiated GAERS (GAERS-SI) (D). **(E)** Global input to L2/3 starter neurons. **(F)** Input to L2/3 distribution among cortical layers. **(G)** Scheme describing the spatial distribution of starter cells and their presynaptic neurons. **(H)** Heat map representing the distribution of pre-synaptic neurons to L2/3 starter neurons in the antero-posterior axis for Control rats and GAERS. Color scale represents the input-to-starter ratio. **(I)** Statistical comparison of the distribution of pre-synaptic neurons to L2/3 starter neurons in the antero-posterior axis for Control rats and GAERS. Color scale represents statistical significance. Bin size is 80 µm. **(J)** Heat map representing the distribution of pre-synaptic neurons to L2/3 starter neurons in the antero-posterior axis for GAERS and GAERS-SI. Color scale represents the input-to-starter ratio. **(K)** Statistical comparison of the distribution of pre-synaptic neurons to L2/3 starter neurons in the antero-posterior axis for GAERS and GAERS-SI. Color scale represents statistical significance. Bin size is 80 µm. (box-and-whisker plots show interquartile interval, median, minimum, maximum and mean as +, N=5 Control, 4 GAERS and 3 GAERS-SI, * $p \leq 0.05$, ** $p \leq 0.01$, Mann-Whitney test (E) and 2-way ANOVA, Tukey's correction for multiple comparison (F,I,K)).

Figure 2: Tracing of L5/6 neuronal connectivity in wS1.

(A-C) Right: Examples of coronal sections showing Starter cell zone in L5/6 with lentivirus-only infected cells (green), starter cells (yellow) and their first-order presynaptic partners (red). Left: Insets in starter cell zone with arrowheads pointing to starter cells. Scale bars: 200 µm (main panels) and 50 µm (insets). For Control (A), GAERS (B) and GAERS-SI (C). **(D)** Global input to L5/6 starter neurons. **(E)** Input to L5/6 distribution among cortical layers. **(F)** Scheme describing the spatial distribution of starter cells and their presynaptic neurons. **(G)** Heat map representing the distribution of pre-synaptic neurons to L5/6 starter neurons in the antero-posterior axis for Control rats and GAERS. Color scale represents the input-to-starter ratio. **(H)** Statistical comparison of the distribution of pre-synaptic neurons to L5/6 starter neurons in the antero-posterior axis for Control rats and GAERS. Color scale represents statistical significance. Bin size is 80 µm. **(I)** Heat map representing the distribution of pre-synaptic neurons to L5/6 starter neurons in the antero-posterior axis for GAERS and GAERS-SI. Color scale represents the input-to-starter ratio. **(J)** Statistical comparison of the distribution of pre-synaptic neurons to L2/3 starter neurons in the antero-posterior axis for GAERS and GAERS-SI. Color scale represents statistical significance. Bin size is 80 µm. (box-and-whisker plots show interquartile interval, median, minimum, maximum and mean as +, N=4 Control, 5

GAERS and 4 GAERS-SI, * p≤0.05, ** p≤0.01, **** p≤0.0001, Mann-Whitney test (D) and 2-way ANOVA, Tukey's correction for multiple comparison (E,H,J)).

Figure 3: RABV monosynaptic retrograde tracing identification of GABAergic connectivity.

(A) Coronal section showing a GABA presynaptic neuron (mCherry+/GABA+, arrowhead). Scale bar: 20 µm. **(B)** GABAergic input distribution among cortical layers for L2/3 starter cells. **(C)** GABAergic input distribution among cortical layers for L5/6 starter cells. (box-and-whisker plots show interquartile interval, median, minimum, maximum and mean as +; L2/3: N=5 Control, 4 GAERS and 3 GAERS-SI; L5/6: N=4 Control, 5 GAERS and 4 GAERS-SI; * p≤0.05, ** p≤0.01, 2-way ANOVA, Tukey's correction for multiple comparison).

Figure 4: Histological effects of cortical microtransections.

(A) Horizontal section showing specific cortical microtransections of wS1 highlighted by NeuN staining (green) loss within the irradiation track. Arrows point to irradiation tracks. **(B)** Example of horizontal sections with neuronal (NeuN) and microvascular (RECA) staining with the quantification of cortical NeuN density and RECA normalized fluorescence intensity (GAERS-SI, N=3 rats, n=3 sections/rats, mean overlaid on individual data). Scale bar represents 100 µm. **(C)** Example of histological staining with the quantification of GFAP fluorescence intensity for GAERS-SI (red) and GAERS (black). (N=3 rats, n=3 sections/rats, for each group; mean overlaid on individual data). Dashed lines represent the irradiation track. Scale bar represents 20 µm. **(D)** Same as (C) for Iba1 staining.

Figure 5: ECoG *in vivo* recordings of wS1 after synchrotron-generated microtransections.

(A) Mean normalized time-frequency maps of SWD of GAERS (left, N= 5 rats, n=30 SWD) and GAERS-SI (right, N=6 rats, n=24 SWD) 8 weeks post-irradiation. Above: examples of SWD. Arrowhead point to fundamental and first harmonic frequencies of SWD. **(B)** Mean normalized power of fundamental frequency of SWD (6-8 Hz) (n≥24 SWD; * p≤0.05, ** p≤0.01, 2-way ANOVA test). **(C)** Schematic drawing of SWD pattern and corresponding parameters. **(D-F)** Characterization of the waveform of the spike component of SWD (Positive slope, negative slope, half duration and total duration) at 2 weeks (D), 4 weeks (E) and 8 weeks post-irradiation (F). (n≥25 spikes; * p≤0.05, ** p≤0.01, Mann-Whitney test). (box-and-whisker plots show interquartile interval, median, minimum, maximum and mean as +, N=5 GAERS and 6 GAERS-SI).

Figure 6: Intracortical *in vivo* silicon probes recordings of wS1 after synchrotron-generated microtransections.

(A) Example of SWD recorded across cortical layers with 16-contact linear silicon probes. Red square: first epileptic spike as analyzed in B. **(B)** Example current source density maps computed for the first spike of SWD centered on the peak of the spike (average of 10 spikes). **(C)** Example of intracortical recorded SWD (upper black trace), corresponding MUA activity (lower black trace) and raster plot (red trace). **(D-E)** MUA activity during (D) and between SWD (E). **(F)** Distributions of mean MUA probability among cortical layers centered on the peak of epileptic spikes. R^2 represents the Gaussian fitting coefficient. **(G-I)** Latency of maximum MUA activity to peak of LFP epileptic spike. (box-and-whisker plots show interquartile interval, median, minimum, maximum and mean as +; N=5 GAERS and 6 GAERS-SI; * $p \leq 0.05$, Mann-Whitney test).

FIGURE 1

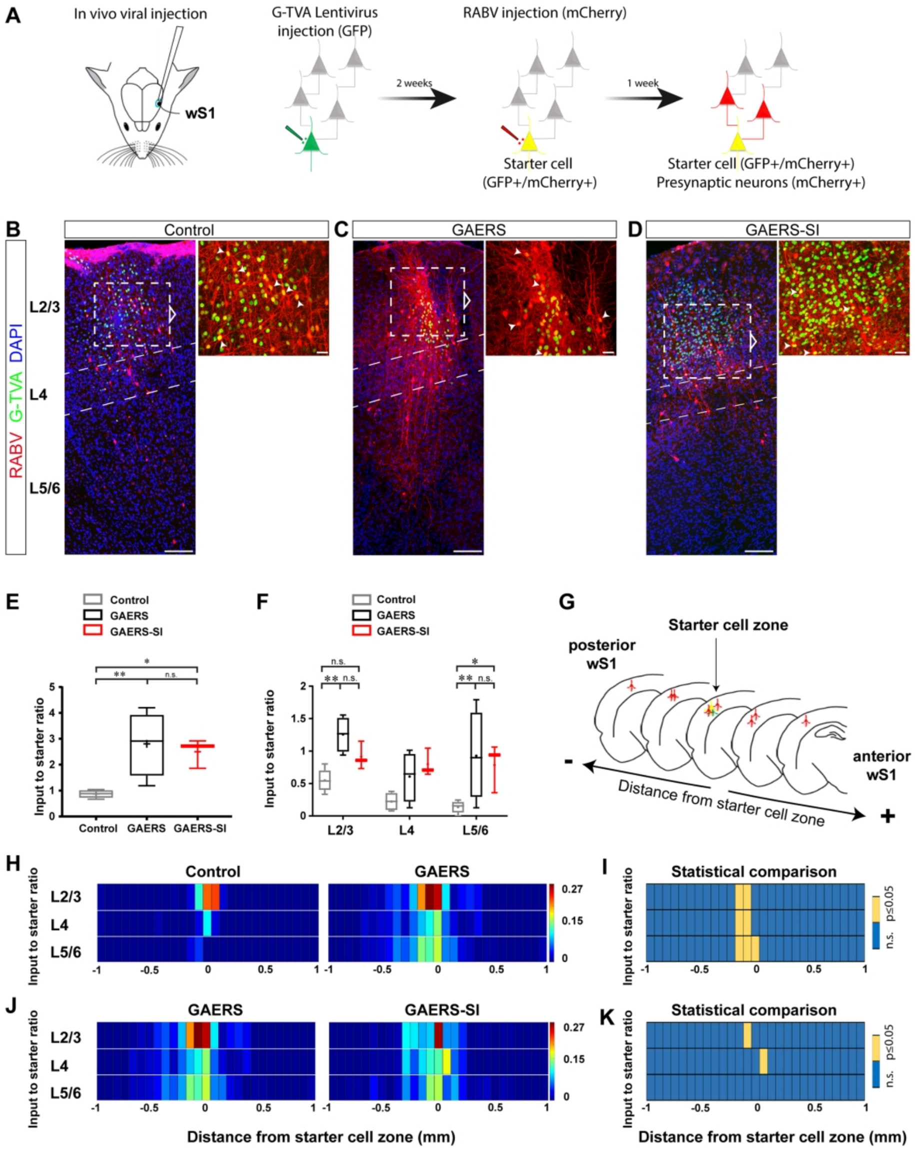

Figure 1: RABV monosynaptic retrograde tracing of L2/3 neuronal connectivity in wS1.
(A) Experimental procedure for tracing monosynaptic inputs to wS1 by injection of G-TVA expressing lentivirus followed by RABV. (B-D) Right: Examples of coronal sections showing starter cell zone in L2/3 with lentivirus-only infected cells (green), starter cells (yellow) and their first-order presynaptic partners (red). Left: Insets in starter cell zone with arrowheads pointing to starter cells. Scale bars: 200 µm (main panels) and 50 µm (inset). For Control (B), GAERS (C) and synchrotron-irradiated GAERS (GAERS-SI) (D). (E) Global input to L2/3 starter neurons. (F) Input to L2/3 distribution among cortical layers. (G) Scheme describing the spatial distribution of starter cells and their presynaptic neurons. (H) Heat map representing the distribution of pre-synaptic neurons to L2/3 starter neurons in the antero-posterior axis for Control rats and GAERS. Color scale represents the input-to-starter ratio. (I) Statistical comparison of the distribution of pre-synaptic neurons to L2/3 starter neurons in the antero-posterior axis for Control rats and GAERS. Color scale represents statistical significance. Bin size is 80 µm. (J) Heat map representing the distribution of pre-synaptic neurons to L2/3 starter neurons in the antero-posterior axis for GAERS and GAERS-SI. Color scale represents the input-to-starter ratio. (K) Statistical comparison of the distribution of pre-synaptic neurons to

L2/3 starter neurons in the antero-posterior axis for GAERS and GAERS-SI. Color scale represents statistical significance. Bin size is 80 µm. (box-and-whisker plots show interquartile interval, median, minimum, maximum and mean as +, N=5 Control, 4 GAERS and 3 GAERS-SI, * p≤0.05, ** p≤0.01, Mann-Whitney test (E) and 2-way ANOVA, Tukey's correction for multiple comparison (F,I,K)).

212x271mm (300 x 300 DPI)

FIGURE 2

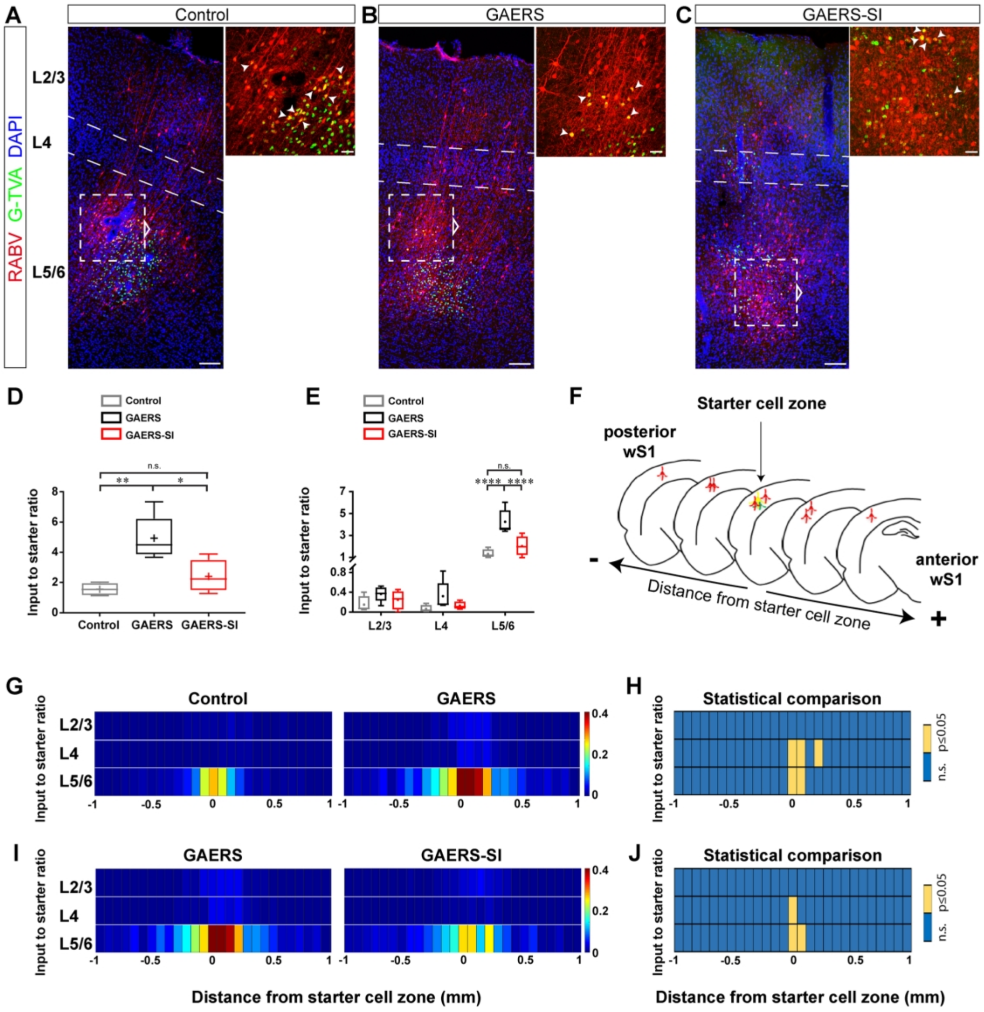

Figure 2: Tracing of L5/6 neuronal connectivity in wS1.
(A-C) Right: Examples of coronal sections showing Starter cell zone in L5/6 with lentivirus-only infected cells (green), starter cells (yellow) and their first-order presynaptic partners (red). Left: Insets in starter cell zone with arrowheads pointing to starter cells. Scale bars: 200 μm (main panels) and 50 μm (insets). For Control (A), GAERS (B) and GAERS-SI (C). (D) Global input to L5/6 starter neurons. (E) Input to L5/6 distribution among cortical layers. (F) Scheme describing the spatial distribution of starter cells and their presynaptic neurons. (G) Heat map representing the distribution of pre-synaptic neurons to L5/6 starter neurons in the antero-posterior axis for Control rats and GAERS. Color scale represents the input-to-starter ratio. (H) Statistical comparison of the distribution of pre-synaptic neurons to L5/6 starter neurons in the antero-posterior axis for Control rats and GAERS. Color scale represents statistical significance. Bin size is 80 μm. (I) Heat map representing the distribution of pre-synaptic neurons to L5/6 starter neurons in the antero-posterior axis for GAERS and GAERS-SI. Color scale represents the input-to-starter ratio. (J) Statistical comparison of the distribution of pre-synaptic neurons to L2/3 starter neurons in the antero-posterior axis for GAERS and GAERS-SI. Color scale represents statistical significance. Bin size is 80 μm. (box-and-whisker plots show interquartile interval, median, minimum, maximum and mean as +, N=4 Control, 5 GAERS and 4 GAERS-SI, * p≤0.05, ** p≤0.01, **** p≤0.0001, Mann-Whitney test (D) and 2-way ANOVA, Tukey's correction for multiple comparison (E,H,J)).

210x221mm (300 x 300 DPI)

FIGURE 3

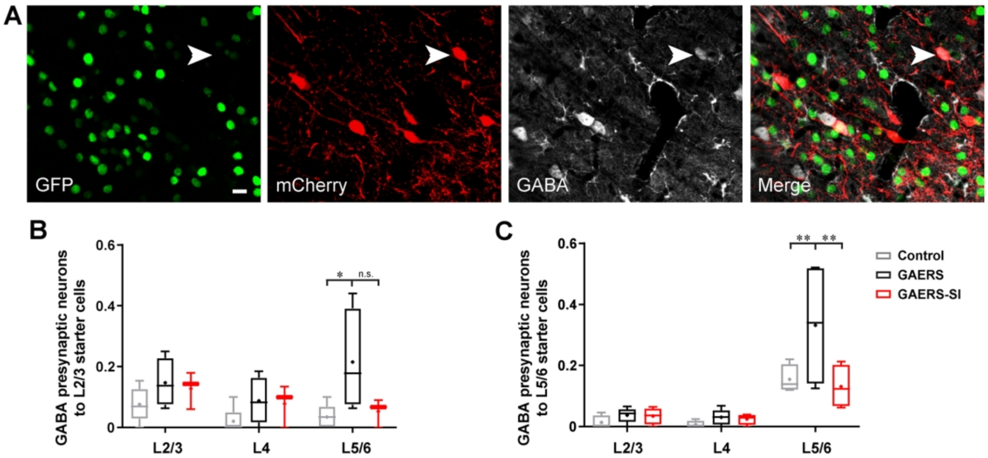

Figure 3: RABV monosynaptic retrograde tracing identification of GABAergic connectivity. (A) Coronal section showing a GABA presynaptic neuron (mCherry+/GABA+, arrowhead). Scale bar: 20 µm. (B) GABAergic input distribution among cortical layers for L2/3 starter cells. (C) GABAergic input distribution among cortical layers for L5/6 starter cells. (box-and-whisker plots show interquartile interval, median, minimum, maximum and mean as +; L2/3: N=5 Control, 4 GAERS and 3 GAERS-SI; L5/6: N=4 Control, 5 GAERS and 4 GAERS-SI; * $p \leq 0.05$, ** $p \leq 0.01$, 2-way ANOVA, Tukey's correction for multiple comparison).

187x92mm (300 x 300 DPI)

FIGURE 4

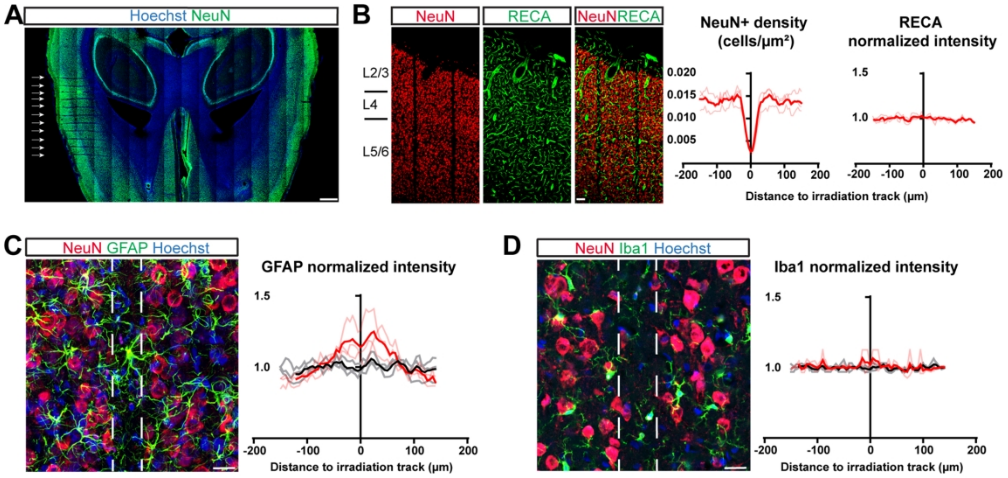

Figure 4: Histological effects of cortical microtransections.
(A) Horizontal section showing specific cortical microtransections of wS1 highlighted by NeuN staining (green) loss within the irradiation track. Arrows point to irradiation tracks. (B) Example of horizontal sections with neuronal (NeuN) and microvascular (RECA) staining with the quantification of cortical NeuN density and RECA normalized fluorescence intensity (GAERS-SI, N=3 rats, n=3 sections/rats, mean overlaid on individual data). Scale bar represents 100 µm. (C) Example of histological staining with the quantification of GFAP fluorescence intensity for GAERS-SI (red) and GAERS (black). (N=3 rats, n=3 sections/rats, for each group; mean overlaid on individual data). Dashed lines represent the irradiation track. Scale bar represents 20 µm. (D) Same as (C) for Iba1 staining.

181x99mm (300 x 300 DPI)

FIGURE 5

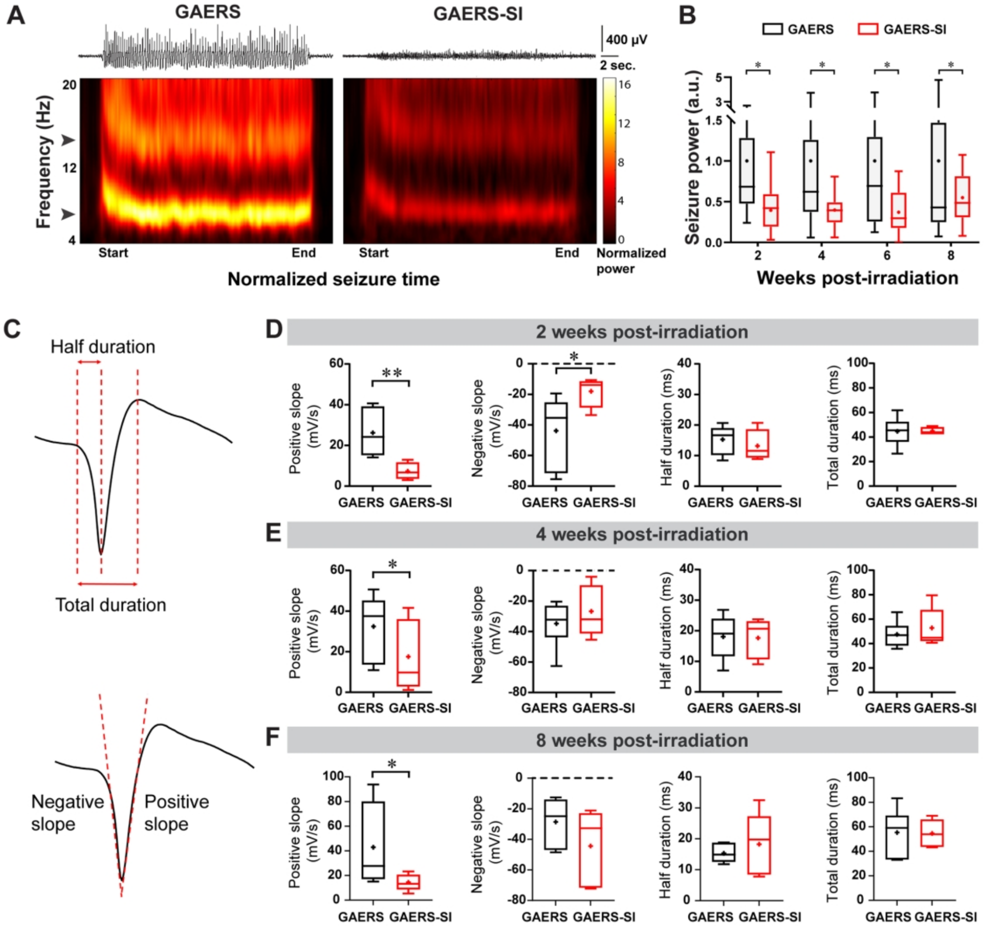

Figure 5: ECoG in vivo recordings of wS1 after synchrotron-generated microtransections. (A) Mean normalized time-frequency maps of SWD of GAERS (left, N= 5 rats, n=30 SWD) and GAERS-SI (right, N=6 rats, n=24 SWD) 8 weeks post-irradiation. Above: examples of SWD. Arrowhead point to fundamental and first harmonic frequencies of SWD. (B) Mean normalized power of fundamental frequency of SWD (6-8 Hz) (n≥24 SWD; * p≤0.05, ** p≤0.01, 2-way ANOVA test). (C) Schematic drawing of SWD pattern and corresponding parameters. (D-F) Characterization of the waveform of the spike component of SWD (Positive slope, negative slope, half duration and total duration) at 2 weeks (D), 4 weeks (E) and 8 weeks post-irradiation (F). (n≥25 spikes; * p≤0.05, ** p≤0.01, Mann-Whitney test). (box-and-whisker plots show interquartile interval, median, minimum, maximum and mean as +, N=5 GAERS and 6 GAERS-SI).

189x188mm (300 x 300 DPI)

FIGURE 6

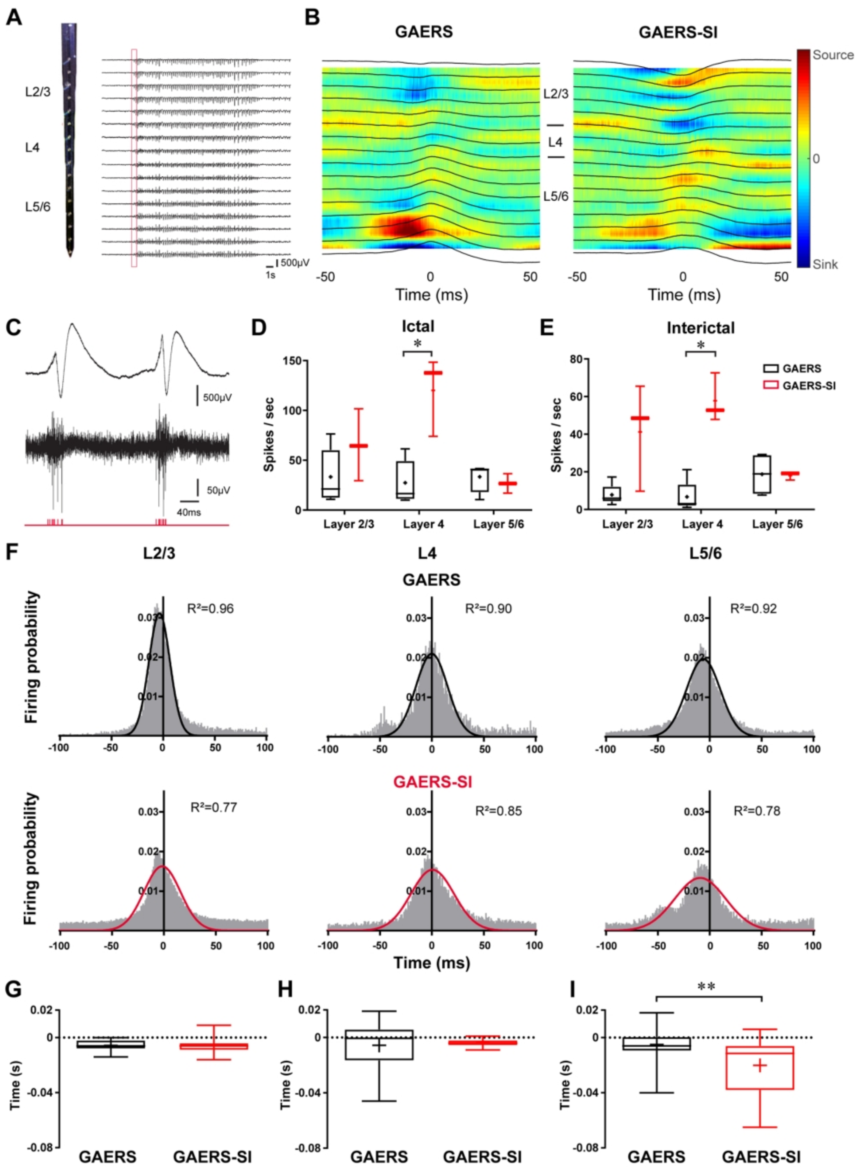

Figure 6: Intracortical in vivo silicon probes recordings of wS1 after synchrotron-generated microtransections.

(A) Example of SWD recorded across cortical layers with 16-contact linear silicon probes. Red square: first epileptic spike as analyzed in B. (B) Example current source density maps computed for the first spike of SWD centered on the peak of the spike (average of 10 spikes). (C) Example of intracortical recorded SWD (upper black trace), corresponding MUA activity (lower black trace) and raster plot (red trace). (D-E) MUA activity during (D) and between SWD (E). (F) Distributions of mean MUA probability among cortical layers centered on the peak of epileptic spikes. R2 represents the Gaussian fitting coefficient. (G-I) Latency of maximum MUA activity to peak of LFP epileptic spike. (box-and-whisker plots show interquartile interval, median, minimum, maximum and mean as +; N=5 GAERS and 6 GAERS-SI; * p≤0.05, Mann-Whitney test).

183x258mm (300 x 300 DPI)

Supplementary material

Supplementary Table 1: List of antibodies

Antibodies	Dilution	Source	Identifier
Mouse monoclonal anti-NeuN (clone A60)	1:500	Merck millipore	Cat# MAB377; RRID:AB_2298772
Rabbit polyclonal anti-CDP	1:250	Santa Cruz Biotechnology	Cat# sc-13024, RRID:AB_2261231
Rabbit polyclonal anti-CTip2	1:250	Abcam	Cat# ab28448, RRID:AB_1140055
Mouse monoclonal anti-RFP	1:500	Abcam	Cat# ab125244, RRID:AB_10973556
Chicken polyclonal anti-GFP	1:250	Abcam	Cat# ab13970, RRID:AB_300798
Rabbit polyclonal anti-GABA	1:250	Sigma-Aldrich	Cat# A2052, RRID:AB_477652
Mouse monoclonal anti-CD68	1:500	Antibodies-Online	Cat# ABIN457478, RRID:AB_10827405
Rabbit polyclonal anti-GFAP	1:500	Agilent Technologies	Cat# Z0334, RRID:AB_10013382
Mouse monoclonal anti-RECA	1:500	Bio-Rad	Cat# MCA970R, RRID:AB_10015280
Mouse monoclonal anti-NEFH	1:1000	Thermo Fischer Scientific	Cat# MA1-2012, RRID:AB_347005
Mouse monoclonal anti-Olig2	1:500	Abcam	Cat# ab56643, RRID:AB_944547
Donkey polyclonal anti-chicken FITC	1:500	Jackson ImmunoResearch Labs	Cat# 703-095-155, RRID:AB_2340356
Goat polyclonal anti-rabbit 488	1:500	Thermo Fischer Scientific	Cat# A-11008, RRID:AB_143165
Donkey polyclonal anti-rabbit 555	1:500	Thermo Fischer Scientific	Cat# A-31572, RRID:AB_162543
Donkey polyclonal anti-mouse 555	1:500	Thermo Fischer Scientific	Cat# A-31570, RRID:AB_2536180
Donkey polyclonal anti-mouse 488	1:500	Thermo Fischer Scientific	Cat# A-21202, RRID:AB_141607
Goat polyclonal anti-rabbit 647	1:500	Thermo Fischer Scientific	Cat# A-21244, RRID:AB_2535812

Supplementary Table 2: Details of statistical results

Figure	**Test**	**Test statistic**	**Degree of freedom**	**p value**
Figure 1E				
Control vs. GAERS	One-tailed Mann-Whitney	U=0	n.a.	0.0079
Control vs. GAERS-SI	One-tailed Mann-Whitney	U=0	n.a.	0.0179
GAERS vs. GAERS-SI	One-tailed Mann-Whitney	U=4	n.a.	0.3143
Figure 1F L2/3				
Control vs. GAERS	2-way ANOVA	F(2,27)=14.86	2	<0.0001
	Tukey	q=4.66	27	0.0075
Control vs. GAERS-SI	2-way ANOVA	F(2,27)= 14.86	2	<0.0001
	Tukey	q=2.21	27	0.28
GAERS vs. GAERS-SI	2-way ANOVA	F(2,27)= 14.86	2	<0.0001
	Tukey	q=1.98	27	0.35
Figure 1F L5/6				
Control vs. GAERS	2-way ANOVA	F(2,27)=14.86	2	<0.0001
	Tukey	q=5.196	27	0.0029
Control vs. GAERS-SI	2-way ANOVA	F(2,27)= 14.86	2	<0.0001
	Tukey	q=3.92	27	0.026
GAERS vs. GAERS-SI	2-way ANOVA	F(2,27)= 14.86	2	<0.0001
	Tukey	q=0.82	27	0.83
Figure 1I				
L2/3	2-way ANOVA	F(50,450)=12.97	50	<0.0001
	Tukey	q=8.73 and 7.99	459	<0.0001 and 0.0003
L4	2-way ANOVA	F(50,450)=12.31	50	<0.0001
	Tukey	q=6.98 and 7.3	459	0.0093 and 0.0033
L5/6	2-way ANOVA	F(50,450)=12.28	50	<0.0001
	Tukey	q=9.76, 6.86 and 12.85	459	<0.0001, 0.0136 and <0.0001

Figure 1K				
L2/3	2-way ANOVA	F(50,450)=12.97	50	<0.0001
	Tukey	q=8.07	459	0.0002
L4	2-way ANOVA	F(50,450)=12.31	50	<0.0001
	Tukey	q=8.27	459	0.0001
L5/6	2-way ANOVA	F(50,450)=12.28	50	<0.0001
	Tukey	n.a.	459	n.s.
Figure 2D				
Control vs. GAERS	One-tailed Mann-Whitney	U=0	n.a.	0.0079
Control vs. GAERS-SI	One-tailed Mann-Whitney	U=3	n.a.	0.1
GAERS vs. GAERS-SI	One-tailed Mann-Whitney	U=1	n.a.	0.0159
Figure 2E L5/6				
Control vs. GAERS	2-way ANOVA	F(2,30)=16.7	2	<0.0001
	Tukey	q=11.57	30	<0.0001
Control vs. GAERS-SI	2-way ANOVA	F(2,30)=16.7	2	<0.0001
	Tukey	q=2.66	30	0.16
GAERS vs. GAERS-SI	2-way ANOVA	F(2,30)=16.7	2	<0.0001
	Tukey	q=8.77	30	<0.0001
Figure 2H				
L2/3	2-way ANOVA	F(50,500)=8.67	50	<0.0001
	Tukey	n.a.	510	n.s.
L4	2-way ANOVA	F(50,500)=4.85	50	<0.0001
	Tukey	q=7.45, 6.58 and 6.66	510	0.0019, 0.029 and 0.023
L5/6	2-way ANOVA	F(50,500)=14.8	50	<0.0001
	Tukey	q=9.77 and 10.44	510	<0.0001 and <0.0001

Figure 2J				
L2/3	2-way ANOVA	F(50,500)=8.67	50	<0.0001
	Tukey	n.a.	510	n.s.
L4	2-way ANOVA	F(50,500)=4.85	50	<0.0001
	Tukey	q=6.44	510	0.044
L5/6	2-way ANOVA	F(50,500)=14.8	50	<0.0001
	Tukey	q=10.18 and 9.77	510	<0.0001 and <0.0001
Figure 3B L5/6				
Control vs. GAERS	2-way ANOVA	F(2,27)=5.9	2	0.0075
	Tukey	q=4.76	27	0.049
GAERS vs. GAERS-SI	2-way ANOVA	F(2,27)=5.9	2	0.0075
	Tukey	q=3.77	27	0.21
Figure 3C L5/6				
Control vs. GAERS	2-way ANOVA	F(2,30)=4.19	2	0.025
	Tukey	q=4.9	30	0.0045
GAERS vs. GAERS-SI	2-way ANOVA	F(2,30)=4.19	2	0.025
	Tukey	q=5.6	30	0.0013
Figure 5B				
2weeks	2-way ANOVA	F(1,213)=31.13	1	<0.0001
	Sidak	t=2.93	213	0.011
4weeks	2-way ANOVA	F(1,213)=31.13	1	<0.0001
	Sidak	t=2.93	213	0.011
6weeks	2-way ANOVA	F(1,213)=31.13	1	<0.0001
	Sidak	t=3.027	213	0.011
8weeks	2-way ANOVA	F(1,213)=31.13	1	<0.0001
	Sidak	t=2.198	213	0.029
Figure 5D				
Positive slope	One-tailed Mann-Whitney	U=0	n.a.	0.0048

Negative slope	One-tailed Mann-Whitney	U=2	n.a.	0.019
Figure 5E				
Positive slope	One-tailed Mann-Whitney	U=5	n.a.	0.041
Figure 5F				
Positive slope	One-tailed Mann-Whitney	U=5	n.a.	0.041
Figure 6D L4	Two-tailed Mann-Whitney	U=2	n.a.	0.0317
Figure 6E L4	Two-tailed Mann-Whitney	U=1	n.a.	0.0159
Figure 6I	Two-tailed Mann-Whitney	U=111.5	n.a.	0.001
Supplementary Fig. 1F S1Body				
Control vs. GAERS	2-way ANOVA	F(2,10)=1.5	2	0.27
	Tukey	q=5.76	60	0.0004
Control vs. GAERS-SI	2-way ANOVA	F(2,10)=1.5	2	0.27
	Tukey	q=4.77	60	0.00037
Supplementary Fig. 1H				
L2/3	2-way ANOVA	F(50,450)=12.97	50	<0.0001
	Tukey	q=6.79	459	0.0165
L4	2-way ANOVA	F(50,450)=12.31	50	<0.0001
	Tukey	q=7.17, 7.26, 7.37 and 11.49	459	0.005, 0.0037, 0.0026 and 0.0001
L5/6	2-way ANOVA	F(50,450)=12.28	50	<0.0001
	Tukey	q=7.44, 11.57 and 6.49	459	0.002, <0.0001 and 0.038

n.a. = not applicable

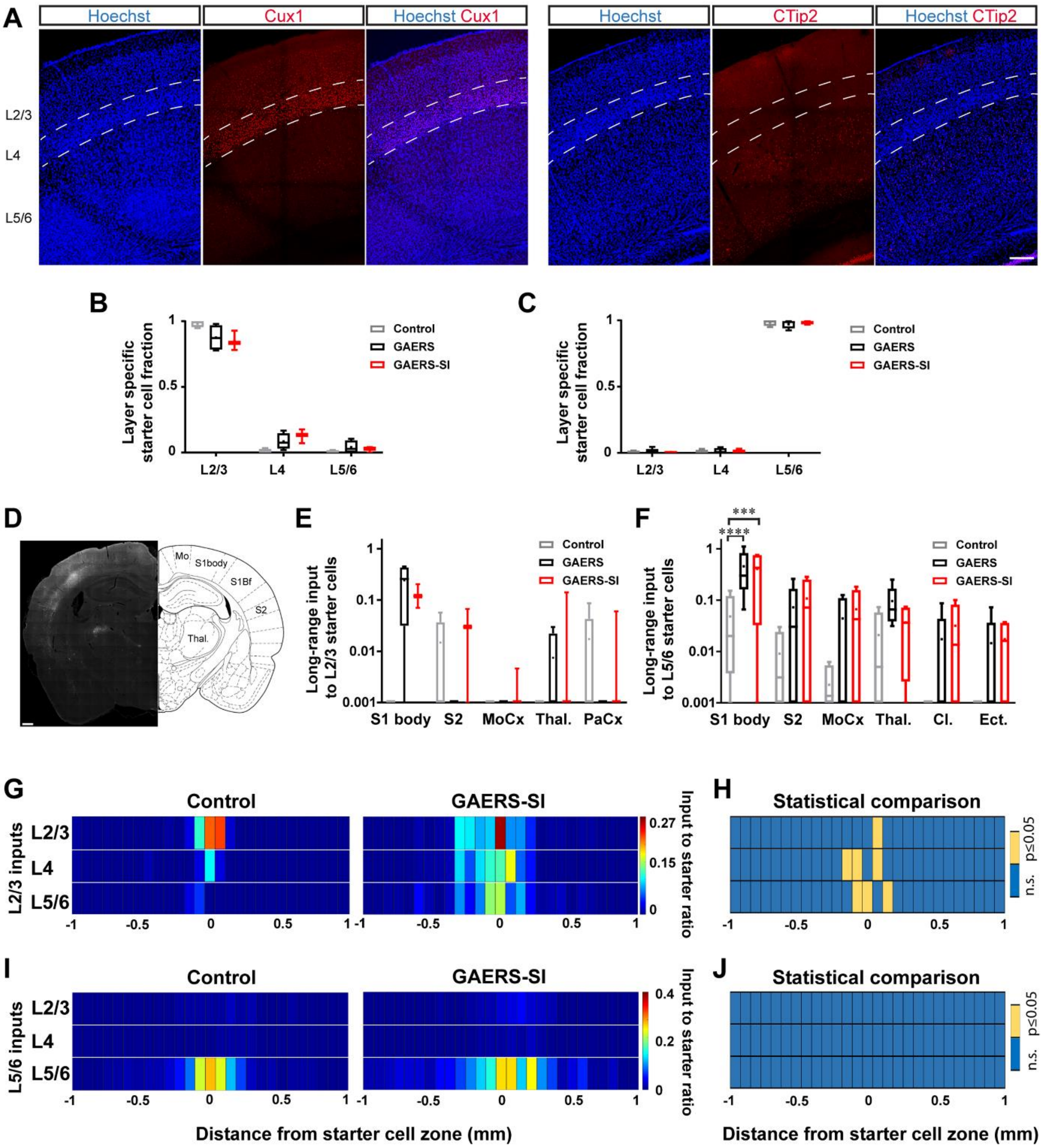

Supplementary Fig. 1: RABV monosynaptic retrograde tracing of wS1 neurons.
(A) Determination of cortical layers boundaries. wS1 layer 4 was determined as the highest density band on Hoechst stained histological sections (blue). Layers above were considered as L2/3 and layers below as L5/6. This was confirmed with Cux1 staining (left, red), a specific marker of superficial (L2/3 and L4) cortical layers, and CTip2 (right, red), a specific marker of deep (L5/6) cortical layers. Scale bar represents 200 µm. White stripes delineate L4. **(B)** Starter cell localization among cortical layers for L2/3 viral injections. **(C)** Starter cell localization among cortical layers for L5/6 viral injections. **(D)** Coronal section and corresponding atlas plates showing presynaptic neurons (white) located in wS1, S1body, S2, Mo and thalamus. Scale bar: 500 µm. **(E)** Distribution of presynaptic neurons to wS1 L2/3 starter cells among brain structures. **(F)** Same as (E) for wS1 L5/6 located starter cells. **(G)** Heat map representing the distribution of pre-synaptic neurons to L2/3 starter neurons in the antero-posterior axis for Control rats and GAERS-SI. Color scale represents the input-to-starter ratio. **(H)** Statistical

comparison of the distribution of pre-synaptic neurons to L2/3 starter neurons in the antero-posterior axis for Control rats and GAERS-SI. Color scale represents statistical significance. Bin size is 80 µm. **(I)** Heat map representing the distribution of pre-synaptic neurons to L5/6 starter neurons in the antero-posterior axis for Control rats and GAERS-SI. Color scale represents the input-to-starter ratio. **(J)** Statistical comparison of the distribution of pre-synaptic neurons to L5/6 starter neurons in the antero-posterior axis for Control rats and GAERS-SI. Color scale represents statistical significance. Bin size is 80 µm. (box-and-whisker plots show interquartile interval, median, minimum, maximum and mean as +; L2/3: N=5 Control, 4 GAERS and 3 GAERS-SI; L5/6: N=4 Control, 5 GAERS and 4 GAERS-SI; *** $p \leq 0.001$, **** $p \leq 0.0001$, 2-way ANOVA, Tukey's correction for multiple comparison).

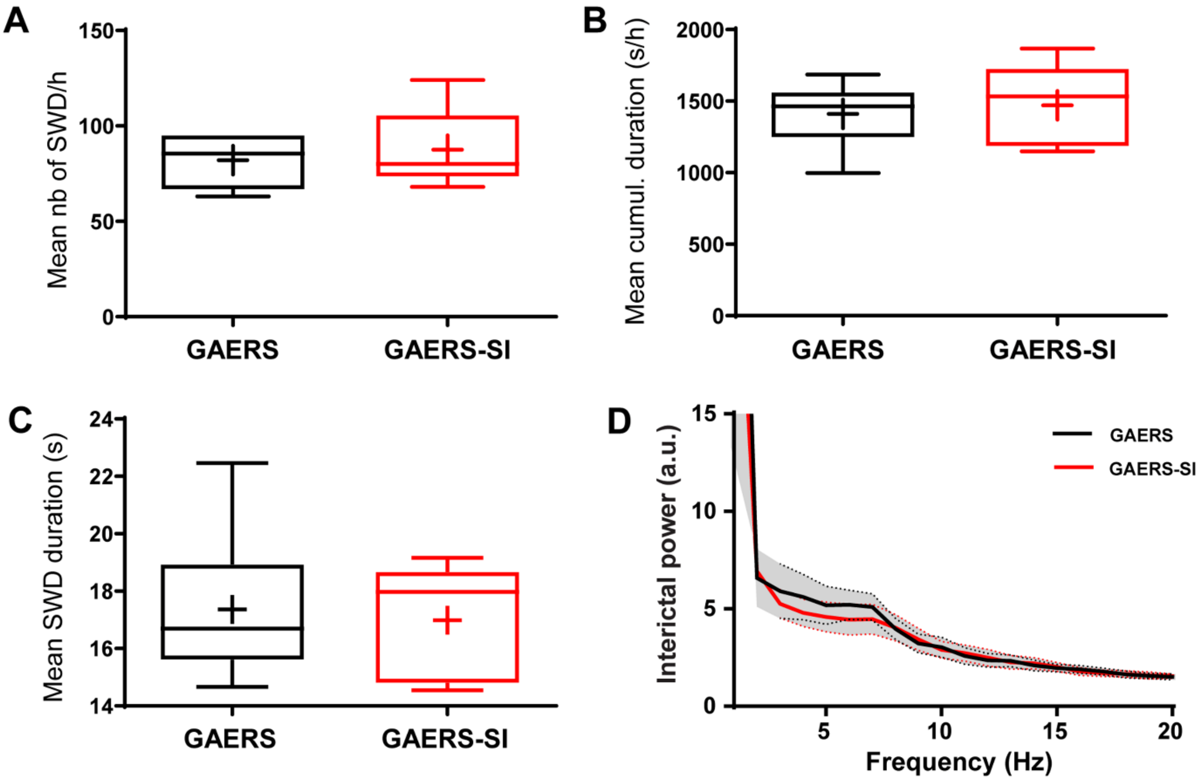

Supplementary Fig. 2: Characteristics of SWD after cortical microtransection.
(A-C) Quantification of SWD number and duration properties 8 weeks after cortical microtransection. **(D)** Mean interictal FFT power 6 weeks after microtransection. (box-and-whisker plots show interquartile interval, median, minimum, maximum and mean as +; N=5 GAERS and 6 GAERS-SI).

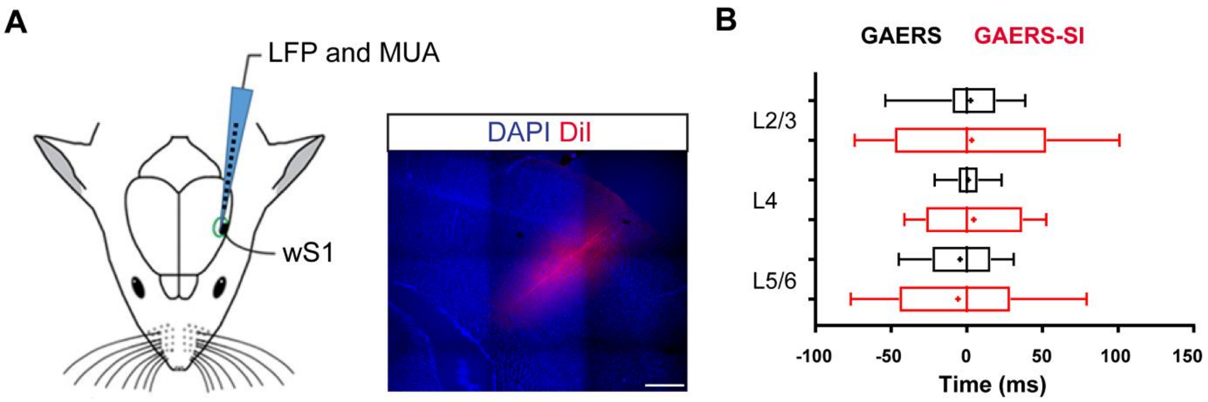

Supplementary Fig. 3: Multi-channel recordings in wS1.
(A) Schematic drawing of experimental set-up. DiI applied on the back of the silicon probe allow post-hoc recording-site localization. Scale bar represents 400 µm. **(B)** Distribution of MUA activity among cortical layers centered on the peak of epileptic spikes (box-and-whisker plots show interquartile interval, median, minimum, maximum and mean as +; N=5 GAERS and 6 GAERS-SI).

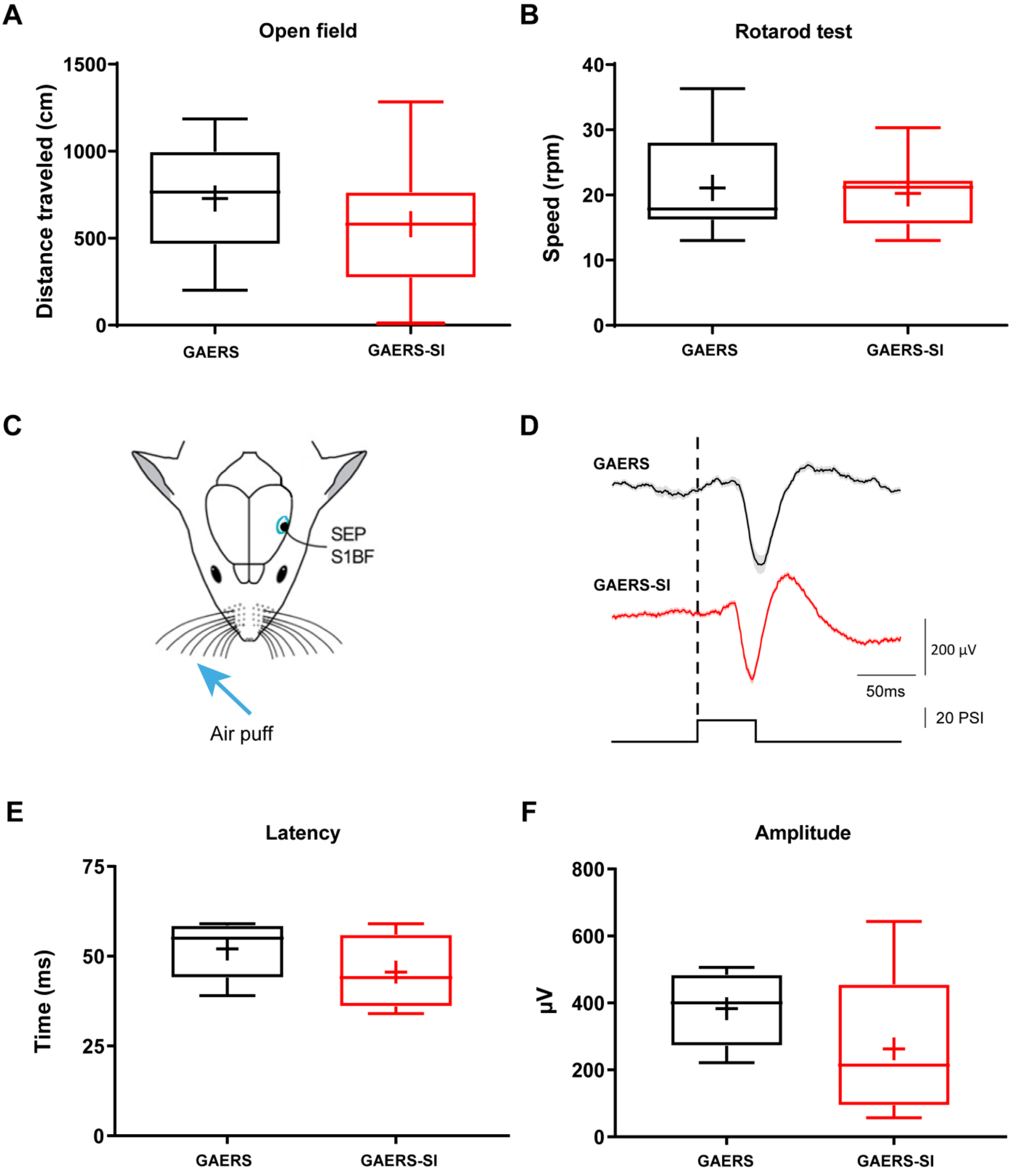

Supplementary Fig. 4: Evaluation of functional side-effects of cortical microtransections. (A) Open field: locomotion performance assessment (N=7 GAERS and 9 GAERS-SI). **(B)** Rotarod test: sensorimotor performance assessment (N=8 GAERS and 10 GAERS-SI). **(C)** Schematic drawing of the experimental preparation allowing air-puff induced Sensory Evoked Potential (SEP) recordings over wS1. **(D)** Example traces of SEP evoked in GAERS (black trace) and GAERS-SI (red trace). Dashed line represents the air-puff delivery onset. **(E)** and **(F)** Latency and amplitude of the peak of SEP after air-puff delivery (N=4 GAERS and 5 GAERS-SI). (box-and-whisker plots show interquartile interval, median, minimum, maximum and mean as +).

The ARRIVE Guidelines Checklist

Animal Research: Reporting In Vivo Experiments

Carol Kilkenny[1], William J Browne[2], Innes C Cuthill[3], Michael Emerson[4] and Douglas G Altman[5]

[1]The National Centre for the Replacement, Refinement and Reduction of Animals in Research, London, UK, [2]School of Veterinary Science, University of Bristol, Bristol, UK, [3]School of Biological Sciences, University of Bristol, Bristol, UK, [4]National Heart and Lung Institute, Imperial College London, UK, [5]Centre for Statistics in Medicine, University of Oxford, Oxford, UK.

	ITEM	RECOMMENDATION	Section/ Paragraph
Title	1	Provide as accurate and concise a description of the content of the article as possible.	title page 1
Abstract	2	Provide an accurate summary of the background, research objectives, including details of the species or strain of animal used, key methods, principal findings and conclusions of the study.	abstract page 1
INTRODUCTION			
Background	3	a. Include sufficient scientific background (including relevant references to previous work) to understand the motivation and context for the study, and explain the experimental approach and rationale. b. Explain how and why the animal species and model being used can address the scientific objectives and, where appropriate, the study's relevance to human biology.	introduction paragraphe 1 and 2
Objectives	4	Clearly describe the primary and any secondary objectives of the study, or specific hypotheses being tested.	introduction paragraphe 3
METHODS			
Ethical statement	5	Indicate the nature of the ethical review permissions, relevant licences (e.g. Animal [Scientific Procedures] Act 1986), and national or institutional guidelines for the care and use of animals, that cover the research.	Materials and methods, section
Study design	6	For each experiment, give brief details of the study design including: a. The number of experimental and control groups. b. Any steps taken to minimise the effects of subjective bias when allocating animals to treatment (e.g. randomisation procedure) and when assessing results (e.g. if done, describe who was blinded and when). c. The experimental unit (e.g. a single animal, group or cage of animals). A time-line diagram or flow chart can be useful to illustrate how complex study designs were carried out.	Materials and methods, section entitled: Rabies virus neuronal connectivity tracing, Synchrotron
Experimental procedures	7	For each experiment and each experimental group, including controls, provide precise details of all procedures carried out. For example: a. How (e.g. drug formulation and dose, site and route of administration, anaesthesia and analgesia used [including monitoring], surgical procedure, method of euthanasia). Provide details of any specialist equipment used, including supplier(s). b. When (e.g. time of day). c. Where (e.g. home cage, laboratory, water maze). d. Why (e.g. rationale for choice of specific anaesthetic, route of administration, drug dose used).	Materials and Methods, in the Surgery subsection of each experimental procedure
Experimental animals	8	a. Provide details of the animals used, including species, strain, sex, developmental stage (e.g. mean or median age plus age range) and weight (e.g. mean or median weight plus weight range). b. Provide further relevant information such as the source of animals, international strain nomenclature, genetic modification status (e.g. knock-out or transgenic), genotype, health/immune status, drug or test naïve, previous procedures, etc.	Materials and methods, section entitled Experimental subjects

The ARRIVE guidelines. Originally published in *PLoS Biology*, June 2010[1]

Housing and husbandry	9	Provide details of: a. Housing (type of facility e.g. specific pathogen free [SPF]; type of cage or housing; bedding material; number of cage companions; tank shape and material etc. for fish). b. Husbandry conditions (e.g. breeding programme, light/dark cycle, temperature, quality of water etc for fish, type of food, access to food and water, environmental enrichment). c. Welfare-related assessments and interventions that were carried out prior to, during, or after the experiment.	Materials and methods, section entitled Experimental subjects
Sample size	10	a. Specify the total number of animals used in each experiment, and the number of animals in each experimental group. b. Explain how the number of animals was arrived at. Provide details of any sample size calculation used. c. Indicate the number of independent replications of each experiment, if relevant.	Materials and methods, section entitled Experimental subjects
Allocating animals to experimental groups	11	a. Give full details of how animals were allocated to experimental groups, including randomisation or matching if done. b. Describe the order in which the animals in the different experimental groups were treated and assessed.	Materials and methods, section entitled
Experimental outcomes	12	Clearly define the primary and secondary experimental outcomes assessed (e.g. cell death, molecular markers, behavioural changes).	Materials and Methods, in
Statistical methods	13	a. Provide details of the statistical methods used for each analysis. b. Specify the unit of analysis for each dataset (e.g. single animal, group of animals, single neuron). c. Describe any methods used to assess whether the data met the assumptions of the statistical approach.	Materials and methods, section entitled Statistical
RESULTS			
Baseline data	14	For each experimental group, report relevant characteristics and health status of animals (e.g. weight, microbiological status, and drug or test naïve) prior to treatment or testing. (This information can often be tabulated).	Materials and methods, section
Numbers analysed	15	a. Report the number of animals in each group included in each analysis. Report absolute numbers (e.g. 10/20, not 50%[2]). b. If any animals or data were not included in the analysis, explain why.	Sections Results, Figure
Outcomes and estimation	16	Report the results for each analysis carried out, with a measure of precision (e.g. standard error or confidence interval).	Sections results,
Adverse events	17	a. Give details of all important adverse events in each experimental group. b. Describe any modifications to the experimental protocols made to reduce adverse events.	Sections Results and Materials and
DISCUSSION			
Interpretation/ scientific implications	18	a. Interpret the results, taking into account the study objectives and hypotheses, current theory and other relevant studies in the literature. b. Comment on the study limitations including any potential sources of bias, any limitations of the animal model, and the imprecision associated with the results[2]. c. Describe any implications of your experimental methods or findings for the replacement, refinement or reduction (the 3Rs) of the use of animals in research.	Discussion, paragraph 1 to 4.
Generalisability/ translation	19	Comment on whether, and how, the findings of this study are likely to translate to other species or systems, including any relevance to human biology.	Discussion, paragraph 5
Funding	20	List all funding sources (including grant number) and the role of the funder(s) in the study.	Subsection entitled

References:
1. Kilkenny C, Browne WJ, Cuthill IC, Emerson M, Altman DG (2010) Improving Bioscience Research Reporting: The ARRIVE Guidelines for Reporting Animal Research. *PLoS Biol* 8(6): e1000412. doi:10.1371/journal.pbio.1000412
2. Schulz KF, Altman DG, Moher D, the CONSORT Group (2010) CONSORT 2010 Statement: updated guidelines for reporting parallel group randomised trials. *BMJ* 340:c332.